The Arizona Radio Observatory CO Mapping Survey of Galactic Molecular Clouds. VI. The Cep OB3 Cloud (Cepheus B and C) in CO J=2-1,

The Astrophysical Journal Supplement Series, 238:20 (24pp), 2018 October https://doi.org/10.3847/1538-4365/aade01

The Arizona Radio Observatory CO Mapping Survey of Galactic Molecular Clouds. VI. The Cep OB3 Cloud (Cepheus B and C) in CO $J = 2$–1, ^{13}CO $J = 2$–1, and CO $J = 3$–2

John H. Bieging[1], Saahil Patel[2], Ryan Hofmann[3], William L. Peters[1], Jouni Kainulainen[4,5], Miaomiao Zhang[5,6], and Amelia M. Stutz[5,7]

[1] Steward Observatory, The University of Arizona, Tucson, AZ 85721, USA
[2] Department of Astronomy, Indiana University, Bloomington, IN 47405-4105, USA
[3] Department of Astrophysical and Planetary Sciences, University of Colorado, Boulder, CO 80309-0391, USA
[4] Dept. of Space, Earth and Environment, Chalmers University of Technology, Onsala Space Observatory, SE-439 92, Onsala, Sweden
[5] Max-Planck-Institut fuer Astronomie, Koenigstuhl 17, D-69117 Heidelberg, Germany
[6] Purple Mountain Observatory & Key Laboratory for Radio Astronomy, Chinese Academy of Sciences, 210008 Nanjing, People's Republic of China
[7] Departmento de Astronomía, Facultad de Ciencias Físicas y Matemáticas, Universidad de Concepción, Concepción, Chile
Received 2018 July 16; revised 2018 August 27; accepted 2018 August 28; published 2018 October 4

Abstract

We present (1) new fully sampled maps of CO and ^{13}CO $J = 2$–1 emission and CO $J = 3$–2 emission toward the molecular clouds Cep B and C, associated with the Cep OB3 association; (2) a map of extinction, A_V, derived from IR colors of background stars; and (3) the distribution of young stellar objects (YSOs) over the same field as the molecular maps. An LTE analysis of the CO and ^{13}CO maps yields the distribution of molecular column densities and temperatures. Substantial variations are evident across the clouds; smaller subregions show correlations between molecular properties and dust extinction, consistent with a picture of outer photodissociation regions with a layer of CO-dark molecular gas, a CO self-shielded interior, and an inner cold dense region where CO is largely depleted onto grains. Comparing the distribution of YSOs with molecular gas surface density shows a power-law relation very similar in slope to that for the giant molecular cloud associated with the H II region Sh2-235 from a previous paper in this series that employed the same methodology. We note the presence of several compact, isolated CO emission sources in the $J = 3$–2 maps. The gas temperature and ^{13}CO velocity dispersion yield a map of the sonic Mach number, which varies across the cloud but always exceeds unity, confirming the pervasiveness of supersonic turbulence over length scales $\gtrsim$0.1 pc (the map resolution). We also compute a $J = 2$–1 CO X-factor that varies with position but is, on average, within 20% of the Galactic average derived from CO $J = 1$–0 observations.

Key words: ISM: clouds – ISM: individual objects (Cepheus B and C – Cep OB3 – Sh2-155) – ISM: kinematics and dynamics – ISM: molecules

Supporting material: data behind figures

1. Introduction

This paper continues a series of large-area molecular cloud mapping studies made with the Heinrich Hertz Submillimeter Telescope on Mt. Graham, Arizona. Previous papers in the series are summarized in Bieging et al. (2016), to which the reader is referred for details.

The target region presented here is the complex of molecular clouds in Cepheus near the Cep OB3 association (Blaauw et al. 1959; Blaauw 1964). The molecular gas was first studied by Sargent (1977, 1979), who subdivided the cloud into regions defined by apparently discrete peaks in the CO distribution, which she designated Cep A, B, C, D, E, and F. More recently, Heyer et al. (1996) presented maps of the $J = 1$–0 transitions of CO and ^{13}CO over a $4° \times 2.°5$ field that includes all of the components identified by Sargent (1977). The Cep A region has been the subject of a number of more recent studies—see Kun et al. (2008) for a summary through 2008 and their Figure 27 for the spatial distribution of the Cep A–F clouds. In this paper, we concentrate on Sargent's regions Cep B and C, which exhibit distinctly different average physical properties and degrees of current star formation. Cep B lies very near several OB stars in the younger subgroup Cyg OB3b (estimated age 4 Myr) and also contains embedded IR and radio continuum sources indicating the presence of newly formed massive stars. The H II region Sh2-155 partially surrounds the Cep B cloud as seen projected on the sky. The Cep C cloud, in contrast, appears to be relatively quiescent in terms of star formation, although recent sensitive near-infrared (NIR) imaging has revealed concentrations of candidate young stellar objects (YSOs) located mainly toward regions of high extinction and large molecular column densities. One bipolar outflow, a sign of current star formation, has also been identified in Cep C (Fukui et al. 1993). The two regions, Cep B and C in Sargent's (1977) designation, are therefore contrasting molecular clouds, of interest for detailed study of their properties and current state of star formation activity.

The distance to the Cep OB3 association has been determined to be 700 pc (Kharchenko et al. 2005). Reid et al. (2014) found a trigonometric parallax distance of 700 pc to a methanol maser source in the Cep A cloud, presumably associated with a massive YSO formed there. Assuming that the B and C cloud components are part of the same molecular cloud complex with Cep A, the maser parallax distance confirms the distance to the stellar association. In this paper, we will assume that the molecular clouds are at a distance of 700 pc with an estimated uncertainty of ±5%.

2. Observations and Data Reduction

2.1. CO and ^{13}CO J = 2–1; CO J = 3–2

Molecular-line observations were made with the Heinrich Hertz Submillimeter Telescope[8] on Mt. Graham, Arizona, at an elevation of 3200 m. The telescope is operated by the Arizona Radio Observatories, a division of Steward Observatory at the University of Arizona.

The $J = 2$–1 rotational transitions of the two most abundant isotopologues, $^{12}C^{16}O$ (hereafter CO) and $^{13}C^{16}O$ (hereafter ^{13}CO), were observed with the sideband-separating mixer receiver (ALMA band 6) described by Lauria et al. (2006). The observing procedures were identical to those described in Bieging et al. (2014). The cloud to be mapped was divided into $10' \times 10'$ "tiles," which were observed with the on-the-fly (OTF) method, and the resulting images were combined to make data cubes of brightness temperature on the sky in a series of spectral channels for each CO isotopologue. The main-beam brightness temperature scale was calibrated by observations of the compact molecular source W3(OH), as described in Bieging & Peters (2011).

The spectrometer had two filter banks, one with 256×1 MHz wide filters and a second with 64×0.25 MHz wide filters. The resulting image cubes were slightly spatially smoothed to give identical angular resolutions for CO and ^{13}CO, with an effective FWHM of $38''$ (corresponding to 0.13 pc at $d = 700$ pc). The velocity axes were resampled to give identical velocity sampling for the two isotopologues to facilitate further analysis. The final data cubes covered the velocity ranges -90 to $+50$ km s^{-1} with a resolution of $\sim$1.3 km s^{-1} for the 1 MHz filters and -30 to $+10$ km s^{-1} with a resolution of 0.325 km s^{-1} for the 0.25 MHz filters.

The $J = 3$–2 transition of CO (but not ^{13}CO) was mapped with a 64-beam focal-plane array receiver, described by Kloosterman et al. (2012). The calibration and observing procedures were the same as those described in Bieging et al. (2016). Because of observing time constraints and differences in procedures, the mapped field was not identical to that of the $J = 2$–1 transition but extended over a larger range in decl. The range of R.A. was further west than in the $J = 2$–1 maps, but not as far to the east, so that the main Cep B region was well covered while the Cep C cloud had less coverage in $J = 3$–2 on the eastern extremity than the $J = 2$–1 map. After modest spatial smoothing, the final $J = 3$–2 map had a spatial resolution of $31''$ (FWHM), corresponding to a spatial resolution of 0.11 pc at $d = 700$ pc. The velocity resolution was 0.233 km s^{-1} spanning -30 to $+10$ km s^{-1} (LSR). The intensities were calibrated in main-beam brightness temperature as described in Bieging et al. (2016). The rms noise in the smoothed maps was 0.235 K for line-free channels.

2.2. Extinction Map from JHK_S Photometry

We obtained NIR JHK_S-band images of the Cep OB3 region on 2011 August 5–7 with the Omega2000 instrument (Kovacs et al. 2004) at the 3.5 m telescope of the Calar Alto Observatory. The Omega2000 camera provides a $15\farcm4 \times 15\farcm4$ field of view with a $0\farcs45$ pixel scale. The observations were conducted in seven partly overlapping fields that covered an $\sim 90' \times 15'$ region. The exposure times of each field were about 35, 41, and 18 minutes for the J, H, and K_S bands, respectively. The weather conditions during the observations were clear, and seeing was between $0\farcs9$ and $1\farcs5$.

The data reduction followed the typical NIR data reduction scheme including dark subtraction, flat fielding using twilight flats, sky subtraction using a mean of temporally neighboring frames, and image registration. The steps were performed with the IRAF[9] software package. The images were registered onto the world coordinate system via comparison to the positions of the 2MASS stars in the fields using IRAF package *imwcs*. We performed source detection and aperture photometry of the sources in the field using the SExtractor software (Bertin & Arnouts 1996).

We used the JHK_S-band data in conjunction with the color-excess mapping technique NICEST (Lombardi 2009) to derive the dust extinction through the observed field. For a detailed description of the technique, see Lombardi (2009). In general, the observed colors of stars shining through a molecular cloud are related to the dust extinction via the equation

$$E_{i-j} = (m_i - m_j) - \langle m_i - m_j \rangle_0 = A_j \left(\frac{\tau_i}{\tau_j} - 1 \right),$$

where E_{i-j} is the color excess, A_j is the extinction, and $\langle m_i - m_j \rangle_0$ is the mean intrinsic color of stars, i.e., the mean color of stars in a control field that can be assumed to be free from extinction. The ratio τ_i/τ_j describes the wavelength dependence of reddening, for which we adopt coefficients from Cardelli et al. (1989):

$$\tau_K = 0.64 \times \tau_H = 0.40 \times \tau_J = 0.11 \times \tau_V.$$

Note that the last conversion to visual extinctions is not needed in deriving the extinction map (which is measured in the NIR), but it is needed to estimate gas column densities using the map. Observations in the JHK_S bands yield two color-excess measurements toward each star. In the NICEST technique, these color-excess measurements toward individual stars are first combined using a maximum-likelihood technique, yielding an estimate of extinction A_V^* toward each detected source. These measurements are then used to produce a regularly sampled map by computing the mean extinction in regular intervals (map pixels), using as weights the variance of each extinction measurement and a Gaussian spatial weighting function. The spatial resolution of the map is set by the width of the weighting function. In this work, we chose to use a FWHM width of $36''$.

Ideally, only stars that are located behind the cloud with respect to the observer should be included in the extinction mapping. In practice, some (small) fraction of stars are located between the cloud and the observer, i.e., in the foreground of the cloud. Also, because the Cep OB3 region is actively forming stars, some stars are embedded in the cloud. Both the foreground sources and cloud members should be removed from the extinction mapping. In the case of Cep OB3 ($D \approx 700$ pc), the fraction of foreground sources is expected to be small, and we use σ-clipping (Lombardi & Alves 2001) to remove stars from the data that have extinction values significantly lower than their nearby stars (and hence are probably in the foreground). We apply a 3σ threshold for the

[8] See http://kp12m.as.arizona.edu/smt_docs/smt_telescope_specs.htm for technical specifications.

[9] IRAF is distributed by the National Optical Astronomy Observatories, which are operated by the Association of Universities for Research in Astronomy, Inc., under cooperative agreement with the National Science Foundation.

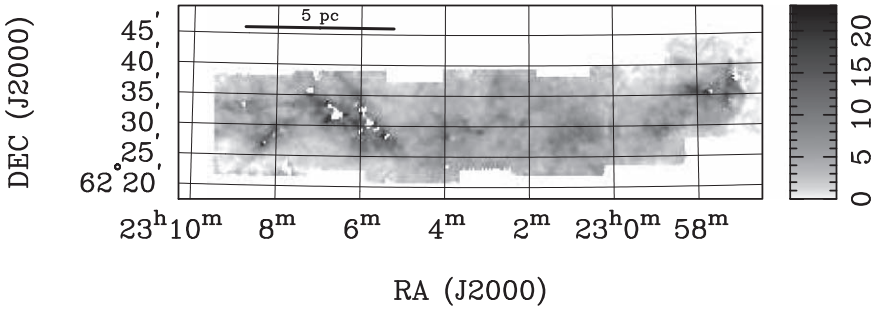

Figure 1. Map of extinction derived from NIR images, expressed as A_V magnitudes. Pixels are blanked where high extinction results in limited star counts and therefore uncertain quantitative values. Effective resolution is 36″.

σ-clipping. To remove the cloud members from the extinction mapping, we used the catalogs of X-ray and mid-infrared identified cloud members by Getman et al. (2006) and Getman et al. (2009), respectively.

Figure 1 shows the resulting dust extinction map of the Cep OB3 cloud. The map spans extinction values up to $A_V \approx 35$ mag at the chosen resolution. Because we made relatively long exposures compared to 2MASS, for example, we are able to achieve a finer angular resolution than has been typical with the NICER method (e.g., Lombardi & Alves 2001) while maintaining sufficient stellar density in each pixel. Only a few pixels in the region are too opaque to have any sources detected in them. The noise properties of this map arising from source counts are similar to most extinction-mapping studies in the literature (e.g., Lombardi & Alves 2001). The uncertainty is about 0.3 mag at low A_V and 1 mag at the highest measurable A_V.

The final NIR extinction map was used to estimate total hydrogen column density, N(H). This was done by first adopting a conversion from NIR extinction to visual extinction (given above) and then adopting a conversion from visual extinction to total hydrogen column density (Bohlin et al. 1978):

$$N(\mathrm{H}) = 2N(\mathrm{H_2}) + N(\mathrm{H\,I}) = (1.9 \times 10^{21}\,\mathrm{cm^{-2}\,mag^{-1}})\ A_V.$$

2.3. Identifying YSOs

We examined archival data from the *Spitzer* IR satellite, including the four bands of the IRAC instrument and the 24 μm MIPS camera, the *WISE* all-sky survey catalog, and the *Herschel* far-IR satellite, to find and classify potential YSOs within the region mapped in CO and ^{13}CO.

In another program subsequent to but separate from the Calar Alto observations described above, we also obtained deep JHK_S images with the Canada–France–Hawaii Telescope (CFHT) observatory on Maunakea and extracted point-source fluxes, which were employed with the longer-wavelength archival data to select YSOs and classify them in the standard evolutionary sequence of Class I, Class II, and flat-spectrum transition disk objects.

The observations were conducted in queue-scheduled observing (QSO) mode between 2012 August and 2012 November with the WIRCam instrument on the CFHT. WIRCam is a NIR mosaic imager with four 2048 × 2048 CCDs, yielding a field of view of $\sim 21' \times 21'$ with a plate scale of $0\farcs306$ pixel^{-1}. We observed 33 fields covering in total an area of $\sim$4 deg^2 toward the Cep OB3 molecular cloud in the J, H, and K_s bands. Each field was imaged with the dithering pattern mode. The individual exposure time was 60 s in the J band, 15 s in the H band, and 23 s in the K_s band. The total integration times of the J, H, and K_s bands for each field were 360, 150, and 138 s, respectively.

Individual images were processed by the CFHT 'I'iwi pipeline (the IDL Interpretor of the WIRCam Images, version 2.1.1), which includes dark subtraction, flat fielding, non-linearity correction, cross-talk removal, and sky subtraction. Absolute astrometry was performed on each single frame by comparing the image with the 2MASS reference catalog (Skrutskie et al. 2006) with SCAMP (Bertin 2006). Based on the accurate astrometry, the dithered individual exposures were combined into the stacked images with the software SWARP (Bertin et al. 2002). Point-source detection and point-spread function (PSF) photometry were performed on the mosaic images via PyRAF, which is a command Python scripting language for running IRAF tasks. Photometric zero points and color terms were calculated by comparison of the instrumental magnitudes of relatively isolated, unsaturated bright sources with the counterparts in the 2MASS Point Source Catalog (Skrutskie et al. 2006). For the point sources, we reach limiting magnitudes of $\sim$20.5, 19.5, and 19 ($\sim 5\sigma$) in the J, H, and K_s images, respectively.

The process of YSO identification is mainly based on the YSO classification schemes presented by Gutermuth et al. (2009) and Koenig & Leisawitz (2014). We also combine several color criteria from Robitaille et al. (2008), Veneziani et al. (2013), and Saral et al. (2015) to isolate the asymptotic giant branch (AGB) stars. The classification method is explained in greater detail in Zhang et al. (2018). The catalog of YSOs will be presented in a separate publication.

The limiting factor in YSO identifications is the sensitivity of the archival *Spitzer* data. The JHK_S data from the CFHT cover a significantly larger area but with a relatively short exposure time compared to the observations at Calar Alto (Section 2.2), which were designed specifically for extinction mapping. Therefore, including the Calar Alto data for YSO identification would have a minimal effect on our catalog completeness.

3. Results

3.1. Global Spectra

The direction to the Cepheus molecular cloud also includes lines of sight to more distant molecular gas associated with the Perseus and "Outer" spiral arms. Figure 2 shows the 1 MHz filter-bank spectrum averaged over the entire mapped field. The strongest feature is at LSR velocities that place it in the Local Spiral Arm, consistent with a distance of 700 pc. Three other weaker features are evident as well, at velocities that place them on the inner and outer parts of the Perseus Arm and Outer Arm. These velocity components have distinctly different

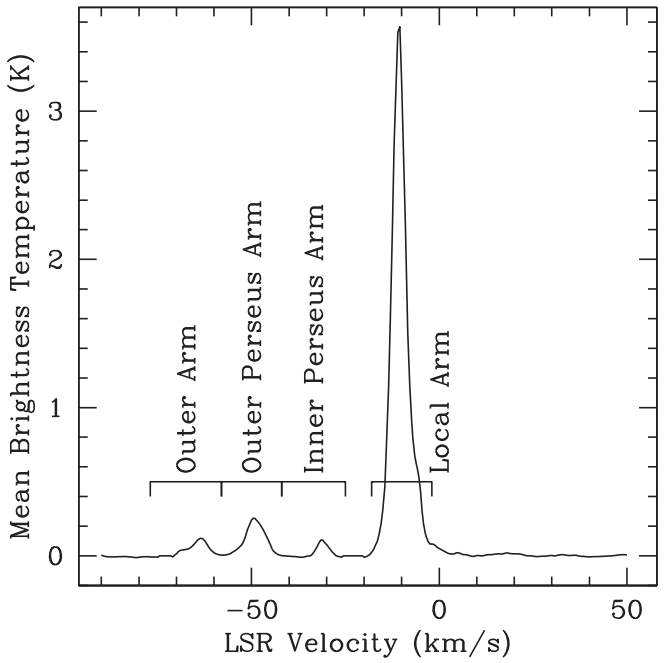

Figure 2. Mean spectrum of CO $J = 2$–1 averaged over the entire field. Horizontal bars mark the velocity ranges of the integrated intensity maps shown in Figure 3.

spatial distributions on the sky. Figure 3 shows the CO $J = 2$–1 intensity integrated over the velocity ranges marked in Figure 2 for the different spiral arm features. The Perseus Arm and Outer Arm maps show several very strong, compact CO emission features, as well as complex structures with mean CO brightness temperatures in the range 10–15 K. (Following Reid et al. 2014, we estimate the distances to these spiral arm features: Inner Perseus Arm, $d \approx 1.6$ kpc; Outer Perseus Arm, $d \approx 2.3$ kpc; Outer Arm, $d \approx 5.6$ kpc; compared with the Cep B and C clouds at $d = 0.7$ kpc.) It is worth noting that far-IR images of thermal dust emission, for example, by the *Herschel* satellite, would not distinguish these kinematic components, so the Outer Arm dust emission features might erroneously be identified as coming from Local Arm dust and gas clouds.

In the remainder of this paper, we will confine our attention to the Local Arm gas in the velocity range from -20 to $\sim+10$ km s^{-1}.

3.2. Maps of CO and ^{13}CO J = 2–1

The Local Arm panel in Figure 3 shows that the molecular cloud has a rather complex structure. Overall, the distribution resembles that of the dust extinction (Figure 1), elongated mainly in the east–west direction. The western end of the CO distribution has a group of three peaks of very strong CO emission (100–150 K km s^{-1}), which corresponds to Sargent's (1977) Cep B component. To the east of Cep B, the CO has a relatively uniform intensity, mainly in the range 30–50 K km s^{-1}. This part of the cloud, Cep C in Sargent's terminology, contains the bulk of the cloud projected area. Though the CO integrated intensity is fairly uniform, there is clearly significant structure within the Cep C region.

To help display this structure, we have made velocity moment maps computed for the velocity range shown in Figure 2 for the Local Arm gas. These are shown in Figure 4, which includes the peak brightness temperature independent of velocity (first panel), the integrated CO intensity (second panel), the first moment or LSR velocity centroid (third panel), and the second moment or velocity dispersion (fourth panel). (The dispersion, σ_V, is related to the FWHM for a Gaussian line shape by a factor of $(8 \ln 2)^{0.5}$, i.e., FWHM $= 2.3548\sigma_V$.) We have divided the cloud into 11 rectangular regions, outlined in Figure 4 and labeled B1–B3 and C1–C8, for the Cep B and C clouds. These regions attempt to select what appear to be physically distinct parts of the clouds, guided mainly by the appearance of the integrated intensity image, as well as the overlap in areal coverage of the extinction map (Figure 1) relative to the CO map. We will examine the average properties of these 11 regions to look for trends in correlations between gas column density, extinction, and related properties in Section 4 below.

The corresponding set of moment maps for the ^{13}CO $J = 2$–1 line is shown in Figure 5. The overall appearance of the peak and integrated intensity maps is very similar to that for the CO isotopologue (Figure 4) but with lower values, as expected for the rarer ^{13}CO. The CO velocity dispersion is significantly wider than that of ^{13}CO, because CO has much larger optical depths than ^{13}CO and therefore much broader lines due to saturation. The map of ^{13}CO velocity dispersion will be used to calculate the sonic Mach number distribution of the mapped area in Section 4.3.

In Figures 6 and 7, we show selected maps of CO and ^{13}CO $J = 2$–1 emission in individual velocity channels. The full velocity range of Local Arm emission is covered. The channel-to-channel variation in morphology is striking. The ^{13}CO integrated intensity (Figure 5), which should be mainly an indicator of total ^{13}CO column density, has some clumpy structure, but not as much as some of the velocity channel maps. The channel-to-channel variation probably therefore reflects turbulent motions in the velocity field, in combination with spatial column density variations.

3.3. Maps of CO J = 3–2

In Figure 8, we show a composite of the velocity moments of the CO $J = 3$–2 line with the integrated intensity, velocity centroid, and velocity dispersion computed for the same range of LSR velocities as the $J = 2$–1 line in Figure 4. The integrated intensity (top panel of Figure 8) is similar to that of the $J = 2$–1 transition in Figure 4, with three strong CO peaks in the westernmost area, Cep B. To the east of R.A. $23^{\rm h}00^{\rm m}$, in the Cep C cloud, the same complex morphology as the $J = 2$–1 line is evident, with a relatively uniform CO intensity of $\sim$30 K km s^{-1} at the brightest positions. The velocity centroid (middle panel of Figure 8) shows little variation in the mean cloud velocity, except for a striking feature near $23^{\rm h}00^{\rm m}30^{\rm s}$, $+62°42'$, which has a centroid velocity that is distinctly different from the bulk of the cloud, redshifted by about 5 km s^{-1}. This feature has the appearance of a large bipolar outflow seen at right angles to the bipolar axis. It is also seen in the CO $J = 2$–1 maps, particularly in CO at velocities of -8.0 and -6.5 km s^{-1} (Figure 6) and in the ^{13}CO velocity centroid map (Figure 5).

The velocity dispersion (bottom panel of Figure 8) ranges mainly between 1 and 2 km s^{-1}, corresponding to a FWHM for a Gaussian profile of $\sim$2.5–5 km s^{-1}. Some isolated regions show larger dispersions, which in some cases result from multiple velocity components on the line of sight, as will be shown in Section 4.

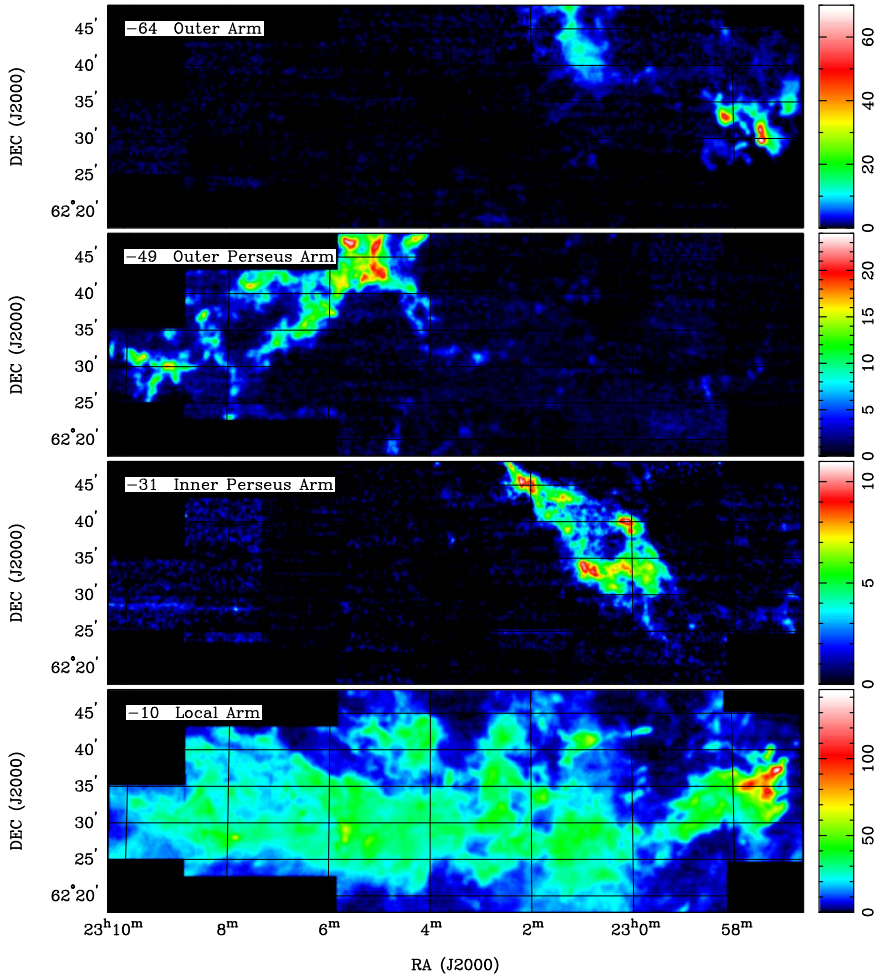

Figure 3. Maps of integrated CO $J = 2$–1 intensity for four velocity ranges corresponding to distinct spiral arms. The velocity ranges are shown in Figure 2. Intensity units are K km s^{-1}. Note that intensity scales are different for each panel. The center LSR velocity is at the upper left with the name of the spiral arm.

Individual channel maps for the CO $J = 3$–2 transition are shown in Figure 9 for selected velocities. The CO distribution closely resembles the corresponding maps for the $J = 2$–1 line, as expected if the molecular levels are populated in near-LTE conditions. We made pixel-by-pixel comparisons of the peak brightness temperature of the $J = 2$–1 and $J = 3$–2 CO maps (after convolving the $J = 3$–2 maps to match the resolution of the $J = 2$–1 image) in the region where they overlap and found that the intensity ratios were consistent with the rotational levels being close to LTE, with the excitation temperature of $J = 3$–2 about 90% of the $J = 2$–1 line. This result was very similar to the case of the Sh2-235 molecular cloud reported in Bieging et al. (2016). With this multitransition comparison as justification, we have used an analysis of the $J = 2$–1 CO and ^{13}CO maps assuming LTE excitation, described in Section 4.

3.4. Isolated CO Features

In an unbiased wide-area survey, features may turn up that show unexpected properties. We found a number of isolated CO emission sources that appear to be unresolved or only slightly resolved in both the CO $J = 2$–1 and $J = 3$–2 maps. Others were detected only in the $J = 3$–2 transition, in the area on the western end that was mapped in $J = 3$–2 but not covered in the $J = 2$–1 map. Since the $J = 3$ level of CO lies 33 K above ground, emission from that line indicates that these isolated clouds must be relatively warm compared to the cold cores with $T \approx 10$ K found in some molecular clouds.

In Table 1, we list the positions, CO $J = 3$–2 line parameters, and inferred sizes of these isolated features. The sizes are from a Gaussian deconvolution. The distances of these isolated features are uncertain but presumably no more than the distance to the Cep B and C clouds, i.e., $<$700 pc. At that distance, the size of a typical $\sim$45″ diameter cloud is $<$0.15 pc. Evidently, these features are at most a few tenths of a parsec in size. The typical line widths are generally smaller than those in the extended molecular clouds but are several times the sound speed if the gas temperature is as high as 30 K, i.e., approximately like the upper-state energy of $J = 3$ ($E/k = 33$ K).

The isolated features listed in Table 1 were selected on the basis of their appearance as distinct, compact emission sources that are present in a few spectral channels and are not blended either spatially or spectrally with more extended CO emission. We include only features that have a peak CO $J = 3$–2 brightness temperature in excess of 1.2 K (5σ). There very likely are similar compact sources that are blended with the spatially extended clouds. The list in Table 1 should be considered a representative sample of such compact clouds, not a complete catalog for the area included in our maps.

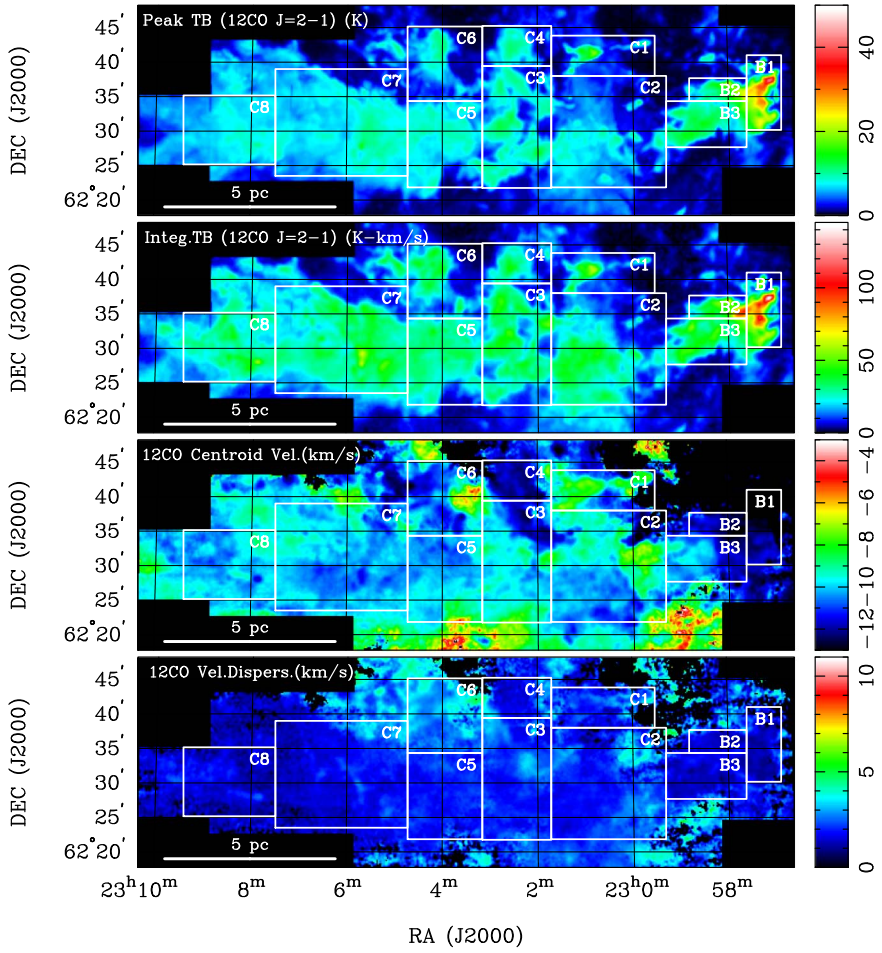

Figure 4. Maps of Local Arm CO $J = 2$–1 peak brightness temperature (K), integrated intensity (K km s^{-1}), centroid LSR velocity (km s^{-1}), and velocity dispersion σ_V (km s^{-1}). For a Gaussian line shape, the line FWHM $= 2.3548\ \sigma_V$. The white boxes show areas defined to examine properties in various subsections of the cloud, labeled for Sargent's (1977) regions B and C.

4. LTE Analysis

We find good agreement in peak brightness temperatures of the $J = 2$–1 and $J = 3$–2 lines of CO when compared pixel by pixel. This agreement is evidence that the lowest rotational levels of CO are populated very nearly in LTE for $J \leqslant 3$. We have used the LTE analysis task *colden*, which is part of the Miriad software package (Sault et al. 1995), to derive CO excitation temperature and molecular column density distributions from the combination of CO and ^{13}CO $J = 2$–1 data cubes. (See Bieging et al. 2016 for details.) We assume that both CO and ^{13}CO have the same excitation temperature, and that the ratio of isotopologue abundance is n(CO)/n(^{13}CO) = 75, where n(X) is the density of molecular species X in molecules cm^{-3}. We estimate the uncertainty in the isotopologue abundance ratio at ±15% (Milam et al. 2005).

The assumptions in our LTE analysis are likely to be satisfied for the denser parts of the molecular gas, which should dominate the sight lines with high extinction. Regions of lower column density gas toward the outer parts of the clouds may have subthermal excitation of the ^{13}CO $J = 2$–1 line. Also, chemical fractionation or selective photodissociation may lower the actual ^{13}CO abundance from what we have assumed. These departures from our assumed LTE conditions would cause an overestimate of the total CO column density. We discuss the uncertainties of this analysis in Section 5.1.

The first panel of Figure 10 shows the distribution of excitation temperature, which closely resembles that of the CO peak brightness temperature, as expected for the optically thick CO line. The second panel of Figure 10 is the optical depth of the ^{13}CO $J = 2$–1 line, which is less than or of order unity almost everywhere in the map. With the assumption that the abundance of ^{13}CO relative to H_2 is 2×10^{-6}, we derived the distribution of molecular hydrogen, shown in the third panel of Figure 10. For comparison, the extinction map discussed in Section 2.3 is shown in the fourth panel.

The labeled rectangles in Figure 10 divide the maps into regions that appear to be physically distinct to some degree. We examine some of the observed and derived properties of these regions, taking spatial averages over the rectangles. In Figure 11, we plot the average CO and ^{13}CO $J = 2$–1 emission spectra. In almost all cases, the profiles are reasonably close to Gaussian, and the CO line does not show obvious indications of self-absorption (i.e., where a minimum or inflection appears at the same velocity as a peak in the ^{13}CO emission). Some of the regions in Cep C show two velocity components, but in these cases, one component that peaks in the range 10–12 km s^{-1} dominates the spectrum. The region C1 is an exception, with two nearly equal components in CO and the lower velocity peak dominant in the ^{13}CO line. Region C1 encloses the feature noted above that appears to be a bipolar outflow seen with its axis nearly in the plane of the sky, so the

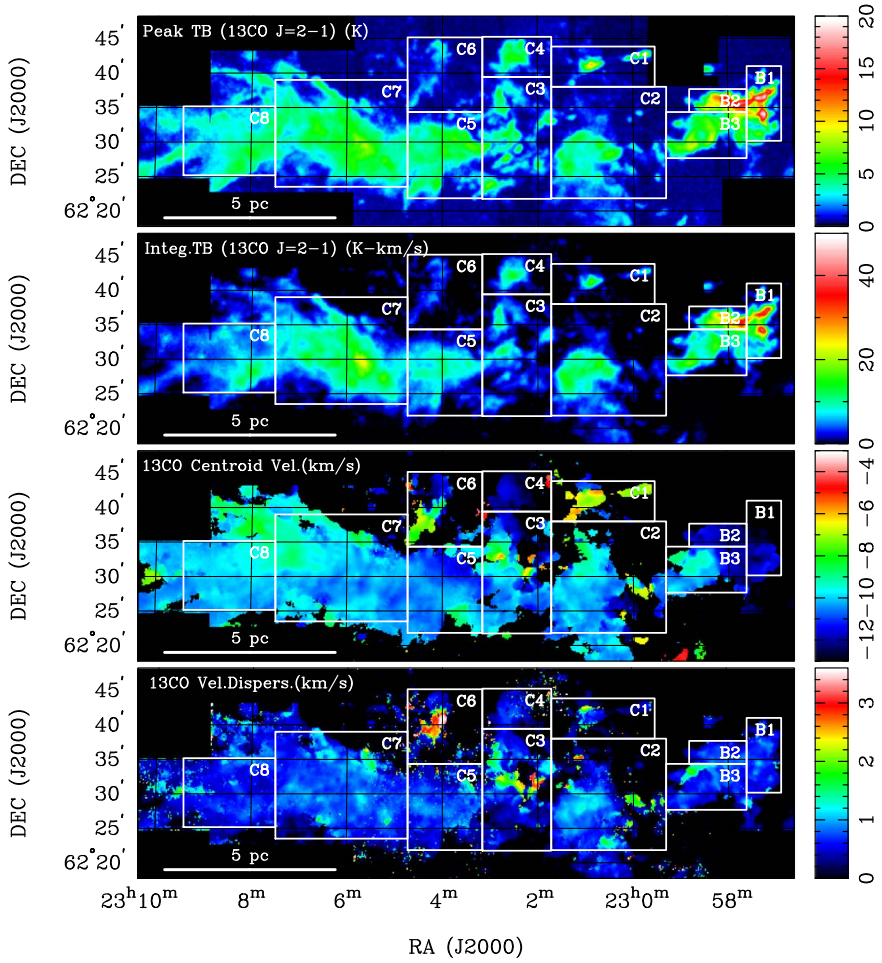

Figure 5. Maps of Local Arm ^{13}CO $J = 2$–1 peak brightness temperature (K), integrated intensity (K km s^{-1}), centroid LSR velocity (km s^{-1}), and velocity dispersion σ_V (km s^{-1}). For a Gaussian line shape, the line FWHM $= 2.3548\sigma_V$. The white boxes show areas defined to examine properties in various subsections of the cloud, labeled for Sargent's (1977) regions B and C.

kinematics of the molecular gas are likely to be different than more typical parts of the cloud complex.

In Table 2, we summarize spatially averaged values from the LTE analysis for the 11 subregions (or "boxes"). The mean ^{13}CO optical depth ranges from 0.21 to 0.61, and the mean excitation temperature (assumed to be the same for both CO and ^{13}CO) is between 12.9 and 27.3 K. The last column lists the total gas mass within each subregion, assuming all the hydrogen is molecular H_2 and including the cosmic abundances of He and heavier elements (a factor of 1.40 times the hydrogen mass). We find that the mean ratio $N(^{13}\mathrm{CO})/A_V$ varies between regions by as much as a factor of 4 between box B1 and C6. (Box C1 is anomalous, since it encloses what appears to be a large bipolar outflow.) Box C6 also has the lowest mean excitation temperature and ^{13}CO optical depth. These variations are likely a result of differences in the cloud structural properties, specifically in the extent of a low-density outer zone containing a photodissociation region (PDR), where the assumptions of our LTE analysis may not be well justified (cf. Section 5.1).

4.1. Gas Column Density Distribution

A key prediction of numerical hydrodynamic models for star formation in molecular clouds is the probability density function of the gas volume density, or ρ-PDF (e.g., Hennebelle & Falgarone 2012; Padoan et al. 2014). Isothermal, non-self-gravitating, nonmagnetized turbulence is expected to have a lognormal ρ-PDF (e.g., Vazquez-Semadeni 1994; Padoan et al. 1997; Federrath et al. 2008). Formation of dense structures within clouds as a consequence of compressible supersonic turbulence may promote star formation under the right circumstances. Turbulent processes coupled with self-gravity may modify an initial lognormal ρ-PDF to show a power-law extension to higher densities as a condition favoring the formation of stars (e.g., Klessen 2000; Kritsuk et al. 2011).

It is not possible, however, to directly infer the three-dimensional ρ-PDF from observations of tracers of the column density distribution of the molecular gas. Several studies have examined the normalized distribution of visual extinction, A_V, in nearby ($d \leqslant 500$ pc) molecular clouds (e.g., Kainulainen et al. 2009, 2011; Schneider et al. 2013; Lombardi et al. 2015). These studies have generally found that only molecular clouds with little current star formation, and perhaps not always then (cf. Lombardi et al. 2015), show lognormal extinction distributions. Rather, most clouds, i.e., clouds with active star formation, showed a power-law-like distribution of column densities. Specifically, Kainulainen et al. (2009), who studied the largest sample of clouds in a homogeneous way, based their study on extinction maps derived from analysis of JHK_S photometry using the NICEST method of Lombardi (2005, 2009), similar to the analysis that produced the map of A_V in Figure 1. In a related

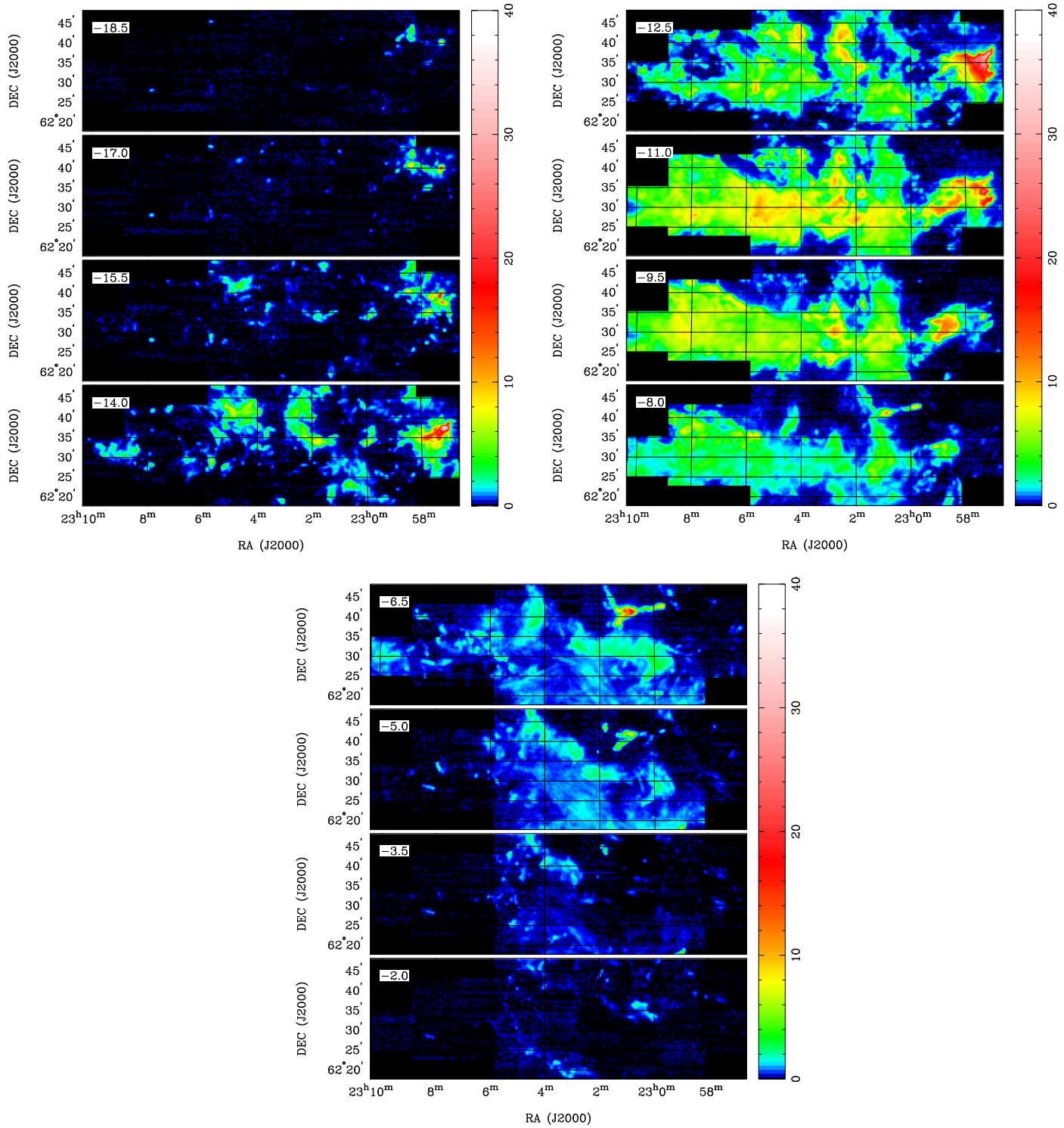

Figure 6. Selected Local Arm channel maps of CO $J = 2$–1 emission. Units are main-beam brightness temperature in K. The color wedge uses a logarithmic stretch to emphasize low surface brightness features. The LSR center velocity is at the upper left, sampled at 1.5 km s^{-1} intervals. The data used to create this figure are available.

study, Kainulainen et al. (2014) developed a modeling approach to constrain the parameters of a lognormal ρ-PDF from measured distributions of visual extinction within molecular clouds or of column density inferred from dust continuum emission.

In this paper, we take a complementary approach by calculating the column density distributions of the molecular gas directly from our LTE analysis of the CO and ^{13}CO maps presented above. In Figure 12, we show (black) histograms of the normalized area as a function of $N(H_2)$ derived from our LTE analysis for the 11 subregions and the entire mapped field. For comparison, we show in red histograms the distribution of our IR-derived A_V map (Figure 1), scaled by the standard

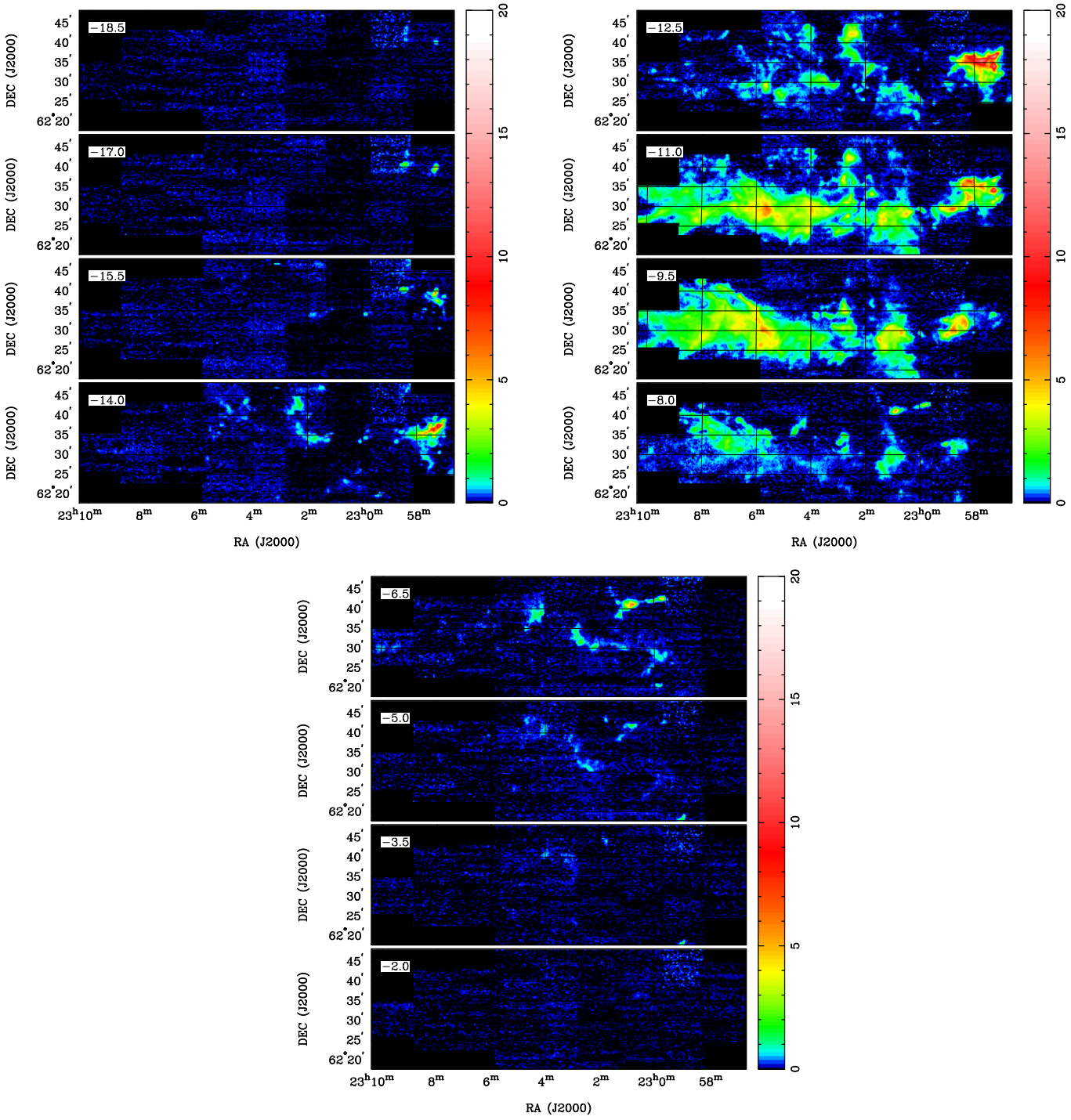

Figure 7. Selected Local Arm channel maps of ^{13}CO $J = 2$–1 emission. Units are main-beam brightness temperature in K. The color wedge uses a logarithmic stretch to emphasize low surface brightness features. The LSR center velocity is at the upper left, sampled at 1.5 km s^{-1} intervals. The data used to create this figure are available.

gas-to-dust factor and assuming all H is molecular. In the lower right panel of Figure 12, we also show in green a lognormal function fitted to the A_V–PDF histogram for $A_V > 3$ mag as an illustrative example. (In this paper, we do not offer a detailed quantitative analysis of the column density PDFs, noting that many of the histograms in Figure 12 are clearly not well described as lognormal in shape.) It is evident that the shape of the distributions varies greatly from one subregion to another. The B1 and B2 regions have the flattest distributions showing the largest fractions of high-density gas. These regions are at the interface between the molecular cloud and the Cep OB3 association, as well as the Sh2-155 H II region; they also show clear signs of massive star formation, with embedded luminous IR sources and ultracompact H II regions (Testi et al. 1995). The other, less active regions in the cloud have steeper PDFs showing lower fractions of high-density gas. This general behavior is similar to several previous studies that have found a strong correlation between the rate of ongoing star formation and the flatness of the PDFs (e.g., Kainulainen et al. 2009, 2014; Lada 2010; Schneider et al. 2013; Stutz & Kainulainen 2015).

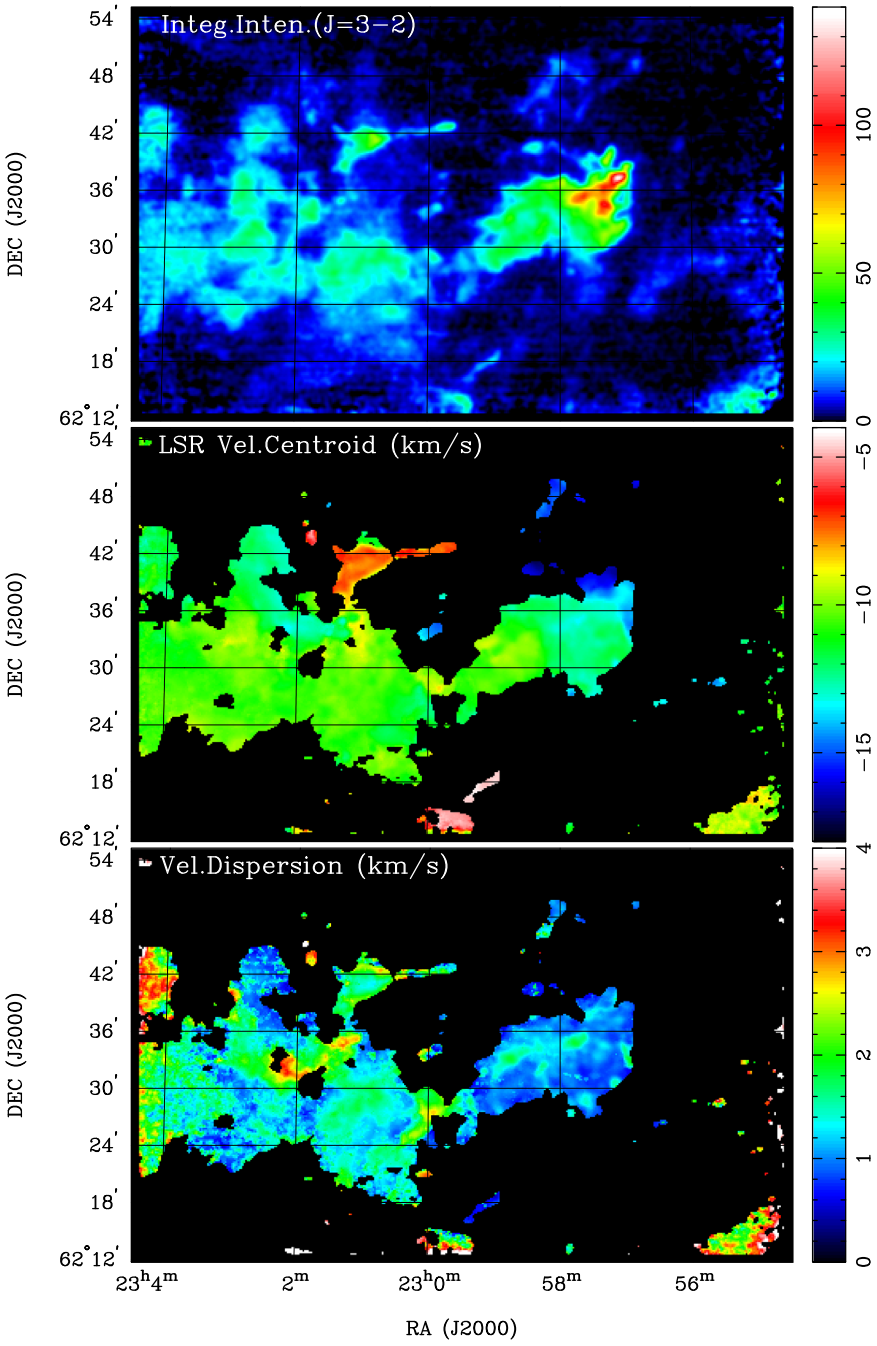

Figure 8. Moments of the CO $J = 3$–2 maps. Integrated intensity (top panel) is in K km s^{-1}. Moments are calculated for the same velocity range as the $J = 2$–1 line in Figure 4.

This trend has been hypothesized to be mainly an effect of the increased role of gravity on the cloud structure (e.g., Kainulainen et al. 2009; Ballesteros-Paredes et al. 2011; Kritsuk et al. 2011; Federrath & Klessen 2013; Burkhart et al. 2015) and also possibly an effect of compression in the regions affected by strong feedback (e.g., Tremblin et al. 2014).

There are some significant differences in the CO- and extinction-based PDFs among the regions. Note that the absolute scaling of both column density measures is quite uncertain, which originates from the uncertainties in the gas-to-dust ratio and H_2-to-CO ratio. Keeping that in mind, the shapes of the CO- and extinction-based PDFs seem to be closer to each other in the B regions than in the C regions. Regions C7 and C8 show the greatest differences between the PDFs of the two tracers, in the sense that the CO-based PDFs exhibit much lower quantities of high column density gas. This difference may be related to freeze-out of CO in the more quiescent regions of the cloud (discussed further in Section 4.2). Our results then indicate that the PDFs derived from CO are susceptible to chemical effects when considering parsec-scale regions of molecular clouds; this conclusion is similar to that recently presented by Schneider et al. (2016).

4.2. Correlation of A_V with Molecular Column Density

It is generally assumed that interstellar gas and dust are well mixed within the galactic disk, and that the ratios of dust to

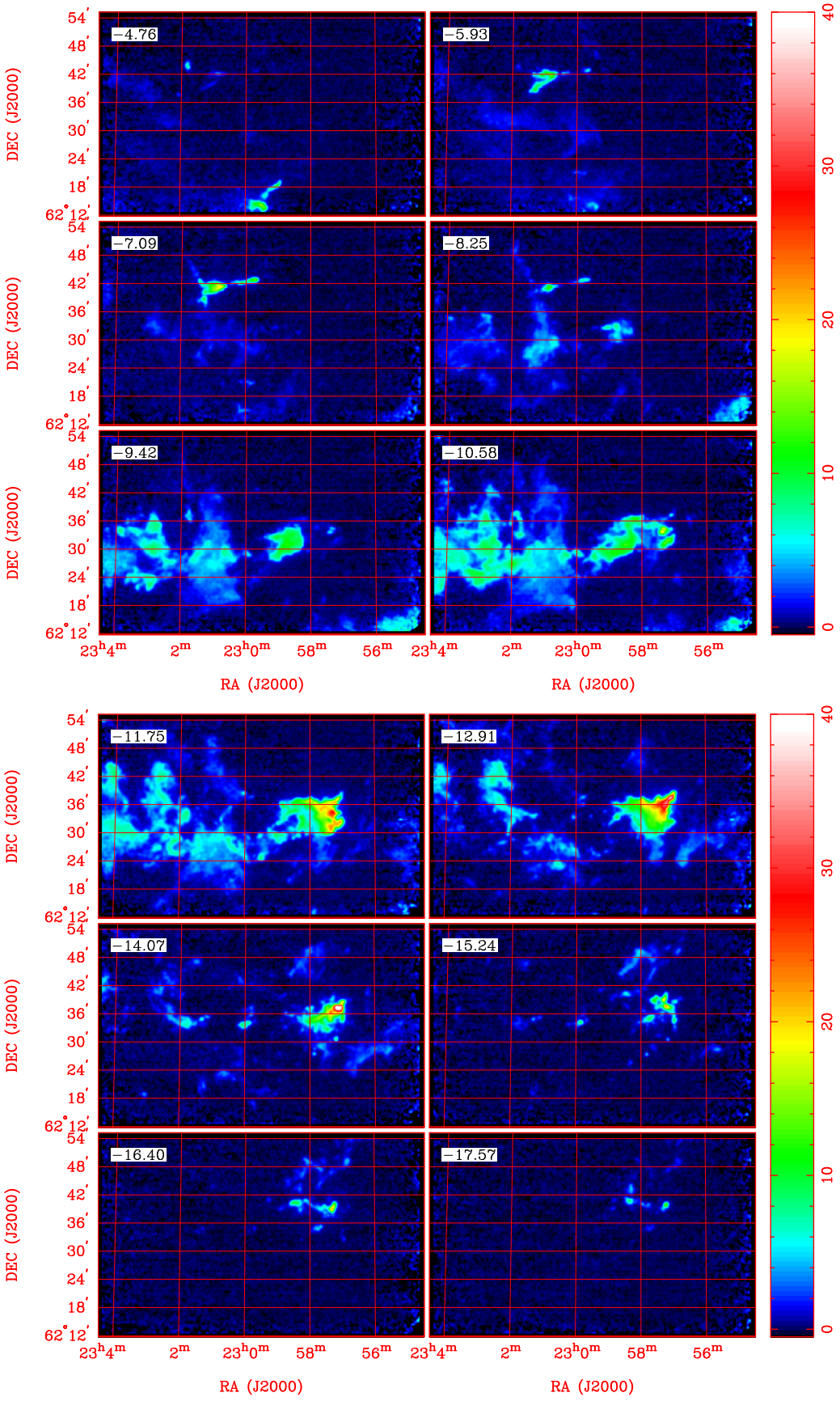

Figure 9. Selected Local Arm channel maps of CO $J = 3$–2 emission. Units are main-beam brightness temperature in K. The color wedge uses a square-root stretch to emphasize low surface brightness features. The LSR center velocity is at the upper left, averaging over five channels, with each channel 0.233 km s^{-1} wide. Note that the area mapped in the $J = 3$–2 line is not the same as that mapped in the $J = 2$–1 lines. The data used to create this figure are available.

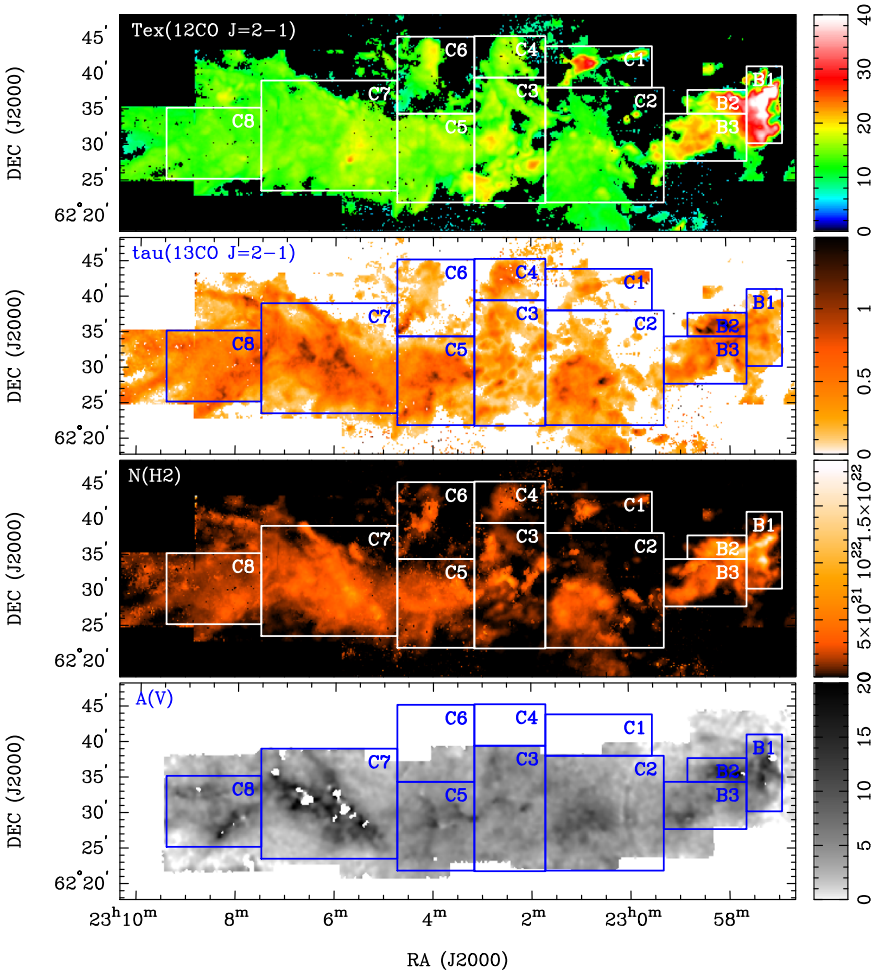

Figure 10. The results of the LTE analysis in the top three panels show CO $J = 2$–1 excitation temperature (in K), ^{13}CO $J = 2$–1 optical depth, and column density of H_2 (in molecules cm^{-2}) compared with visual extinction A_V (bottom panel) in magnitudes derived from NIR photometry of background stars.

Table 1
Isolated Compact CO $J = 3$–2 Sources

V_{LSR}(peak) (km s^{-1})	FWHM (km s^{-1})	R.A. (J2000) h m s	Decl. (J2000) deg arcmin arcsec	Size[a] (arcsec × arcsec)	T_{mb}(peak) (K)
+8.51	1.2	22 58 32.0	62 28 00	⋯	1.48
+5.48	1.4	22 56 19.7	62 28 00	⋯	1.36
+0.13	1.2	23 00 36.0	62 40 12	34 × 25	3.83
−1.04	1.1	23 01 43.7	62 42 49	⋯	2.04
−3.13	1.0	23 00 30.2	62 16 13	44 × 28	3.76
−3.36	1.0	23 00 20.3	62 41 34	42 × 21	1.52
−3.36	1.2	23 01 55.5	62 45 08	33 × 18	3.54
−11.75	1.0	23 00 02.3	62 38 24	63 × 58	5.76
−12.68	1.0	22 59 33.7	62 33 34	47 × 38	1.93
−13.14	1.8	22 58 06.3	62 29 04	58 × 50	2.40
−13.61	3.5[b]	22 57 50.4	62 28 45	73 × 62	3.16
−14.31	1.6	22 57 11.0	62 30 42	55 × 46	6.26
−14.31	2.2	22 57 51.1	62 27 32	47 × 45	3.66
−14.54	1.6	23 01 19.7	62 34 57	62 × 47	5.43
−22.22	1.9	22 56 43.0	62 40 49	51 × 46	3.02
−22.69	1.3	22 55 49.8	62 31 35	44 × 40	3.17
−25.02	0.8	22 57 01.6	62 44 55	55 × 45	1.21

Notes.
[a] Deconvolved Gaussian major and minor diameters; "⋯" means unresolved.
[b] Blended profile.

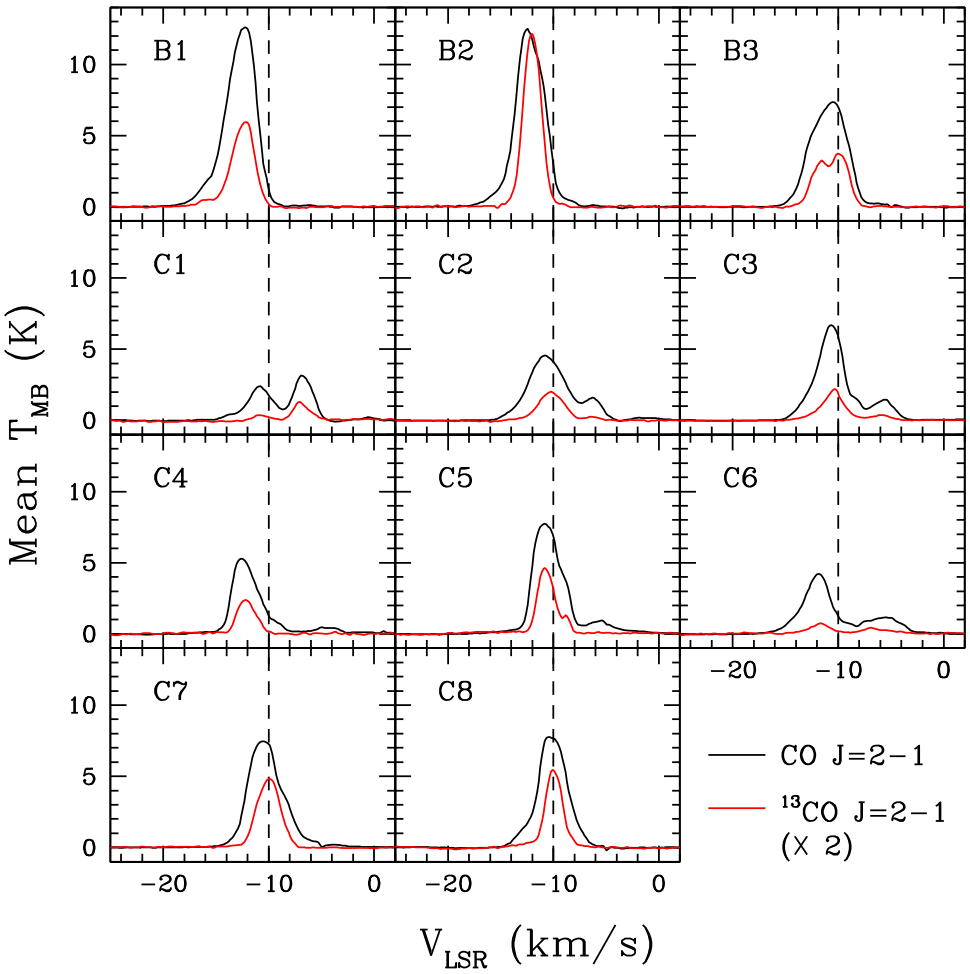

Figure 11. The CO (black) and ^{13}CO (red) $J = 2$–1 spectra averaged over pixels within the subregions shown in Figures 3, 4, and 10. The vertical dashed line serves as a reference marker. The intensity scale of the ^{13}CO spectra is expanded by a factor of 2.

total gas column densities along any sight line are uniform as well, at least within the solar neighborhood. The standard ratio, noted in Section 2.3 above, was derived from observations of UV spectra of hot stars (Bohlin et al. 1978; Rachford et al. 2002), which allowed measurement of the column density of both atomic (H I) and molecular hydrogen, together with the reddening. If these assumptions were correct and all of the gas on a sight line were in molecular form, and the relative abundance of ^{13}CO to H_2 were everywhere the same, we should see a very close correlation between the column density derived from our LTE analysis of the CO and ^{13}CO $J = 2$–1 maps and the extinction, A_V, derived from the NIR analysis of reddening described in Section 2.3.

In Figure 13, we plot the column density of H_2 from our LTE analysis against A_V derived from NIR photometry (cf. Figure 1 and Section 2.3) at each (unblanked) pixel for the 11 subregions, B1–C8. The red line shows the predicted relation from the standard ratio from Bohlin et al. (1978) and extended by Rachford et al. (2002) that would apply if all hydrogen were in molecular form. There are substantial deviations from the nominal relation, both within one subregion and between subregions. The Cep B1 and B2 regions show the highest molecular column density, with maximum values $>1.5 \times 10^{22}$ cm^{-2}. For B1, there is a cloud of points that extends both above and below the red line but with a general trend along it. For B2 and B3, some pixels lie above the nominal relation, but they are mostly below, though the clouds of points generally follow the trend line. In contrast, regions C5, C7, C8, and, to some degree, C3 show an upper envelope consistent with the red line up to $A_V \approx 5$–7 mag but then exhibit a nearly horizontal distribution out to $A_V \sim 20$ mag, with H_2 column densities that appear to be limited to $<5 \times 10^{21}$ cm^{-2}, with pixels at the highest visual extinctions lying well below the red line.

A possible interpretation of the trends seen in subregions C5, C7, and C8 is that at the low temperatures derived from our LTE analysis, at high visual extinction, the CO molecules become frozen out of the gas phase and are deposited on the surfaces of dust grains. If that explanation is correct, then the line-of-sight averaged CO depletion factor can be inferred from the vertical distance of the points below the nominal gas-to-dust ratio shown by the red line. In Figure 13, we plot as blue histograms the depletion factors averaged over 2 mag bins in A_V, where the depletion factor is defined as

$$\text{Depletion factor} \equiv 9.4 \times 10^{20} A_V / N(\text{H}_2).$$

A depletion factor of 4, for example, means that the inferred H_2 column density is 1/4 of the value implied by the standard gas-to-dust ratio and, if all hydrogen were molecular, for the derived value of A_V. In subregion C5, the depletion factor is nearly constant at ~3 up to $A_V = 13$ mag. For C7 and C8, the

Table 2
Spatial Average Properties of Subregions for Cep B and C Clouds

Box	Size (pc)	$\langle\tau(^{13}\mathrm{CO})\rangle$	$\langle T_{ex}(\mathrm{CO})\rangle$ (K)	$\langle N(\mathrm{H_2})\rangle$ (mol cm^{-2})	$\langle N(^{13}\mathrm{CO})/A_V\rangle$ (mol cm^{-2} mag^{-1})	$\langle A_V\rangle$ (mag)	M_{gas}[a] ($M_\odot$)
B1	1.0 × 2.2	0.28	27.3	3.5E+21	1.1E+15	5.1	150
B2	1.7 × 0.7	0.61	20.5	4.7E+21	1.0E+15	7.4	120
B3	2.4 × 1.4	0.40	18.1	2.4E+21	8.2E+14	5.2	150
C1	3.1 × 1.2	0.25	14.5	9.4E+20	1.2E+14	1.9	32
C2	3.4 × 3.3	0.31	13.0	1.3E+21	4.3E+14	4.6	205
C3	2.0 × 3.6	0.24	15.2	1.2E+21	4.2E+14	4.8	150
C4	2.0 × 1.2	0.32	13.9	1.1E+21	…[b]	…[b]	40
C5	2.2 × 2.6	0.42	14.9	1.7E+21	6.1E+14	5.3	200
C6	2.2 × 2.2	0.21	12.9	9.3E+20	2.9E+14	3.1	50
C7	3.9 × 3.2	0.45	14.7	2.1E+21	7.4E+14	5.4	520
C8	2.7 × 2.0	0.46	13.5	1.5E+21	7.0E+14	4.8	190
Total							1807

Notes.
[a] Includes He and heavier elements.
[b] Subregion C4 not included in A_V map.

depletion factors increase with A_V from factors of 2 up to ∼6 at the highest extinction bins ($A_V = 21$ mag).

The freeze-out of CO onto cold dust grains depends on many physical and chemical parameters (see, e.g., Maret et al. 2013) and is also time-dependent, so these line-of-sight integrated quantities cannot be directly related to the gas-phase abundance of CO in the densest interior of the clouds. Maret et al. (2013) found that for prestellar core models, the gas-phase central CO abundance is 2–3 orders of magnitude lower than the peak value. Typical line-of-sight depletion factors of 3–6 in subregions C5, C7, and C8 are therefore not inconsistent with severe CO freeze-out in the densest cloud interiors.

Local variations of the CO-to-A_V ratio have been seen at scales similar to the Cepheus subregions in other nearby molecular clouds (e.g., Kainulainen et al. 2006; Pineda et al. 2008; Kong et al. 2015), and such variations have also been linked to dust temperature variations (e.g., Kainulainen et al. 2006).

4.3. Distribution of Sonic Mach Numbers

The role of supersonic turbulence is crucial in current models of "gravo-turbulent" star formation (e.g., Vazquez-Semadeni 1994; Hennebelle & Falgarone 2012; Padoan et al. 2014; Federrath 2018). The sonic Mach number is a key parameter in numerical simulations of this process, and we can use our LTE analysis to derive the sonic Mach number at each map pixel. Adopting our assumption of LTE, the gas kinetic temperature should equal the CO $J = 2$–1 excitation temperature. We use $T_{\mathrm{ex}} = T_{\mathrm{kin}}$ to derive the isothermal sound speed, $C_s = \sqrt{kT_{\mathrm{kin}}/\mu}$, where $\mu = 2.33$ AMU for molecular hydrogen with helium 10% by number. The one-dimensional line-of-sight velocity dispersion for the ^{13}CO $J = 2$–1 line (σ_v^{1D}) together with C_s gives the sonic Mach number as

$$M_s = \sqrt{3}\,\sigma_v^{1D}/C_s.$$

(We use the velocity dispersion of the optically thin ^{13}CO line because the CO line is generally so optically thick that the line is broadened by radiative transfer effects and so is not a good measure of the internal kinematics of the clouds.)

Figure 14 shows the resulting distribution of sonic Mach numbers using the T_{ex} distribution from Figure 10 and the ^{13}CO velocity dispersion from Figure 5. The range displayed in Figure 14 is truncated at $M_s \leqslant 10$. Pixels with larger values may be affected by second velocity components that distort the ^{13}CO velocity dispersion and so are unreliable. The values of M_s span a range that varies with the subregions defined earlier. In Figure 15, we show histograms of the distribution of the sonic Mach number for the 11 subregions. Regions B1, B2, B3, C1, C7, and C8 show distributions with a clear peak and fairly narrow spread in values of M_s. Regions C2, C3, C4, C5, and C6, in contrast, have broad, relatively flat distributions. In every case, there are very few pixels with $M_s < 1$, so we may infer that at least for length scales exceeding the resolution of the CO maps (0.13 pc), supersonic turbulence permeates the clouds virtually everywhere.

4.4. Comparison with Associated YSOs

The connection between molecular gas column density and the formation of stars is well established (e.g., Kennicutt & Evans 2012). We examine this connection for the Cep B and C clouds by comparing the map of molecular gas column density derived from our LTE analysis of CO and ^{13}CO $J = 2$–1 emission, described in Section 4.1, with the distribution of YSOs identified from IR photometry (Section 2.3). Figure 16 shows the identified Class I YSOs as magenta crosses and Class II YSOs as cyan crosses, all overlaid on the map of total molecular gas surface density in $M_\odot\,\mathrm{pc}^{-2}$, with a logarithmic color stretch to emphasize the lower-level surface density regions. The Class I objects are generally more concentrated on the higher gas surface density regions but constitute only about 20% of all the YSOs shown. The Class II YSOs are more widely distributed. There is a dense concentration of mainly Class II objects in the upper right corner of the map where there is little or no molecular gas. This area coincides with the Cep OB3 association, which has a subcluster with an estimated age of ∼4 Myr. The H II region Sh2-155 is also located at this end of the Cep B cloud. Evidently, the YSOs identified there are young members of the association, but the molecular gas from which they formed has been largely dispersed or dissociated by the hotter members of Cep OB3, which are the ionizing stars of Sh2-155. A second concentration of YSOs is seen centered near R.A. $23^{\mathrm{h}}06^{\mathrm{m}}$, decl. 62°30′, lying mainly within the subregion C7 defined above. The Class I YSOs appear to be

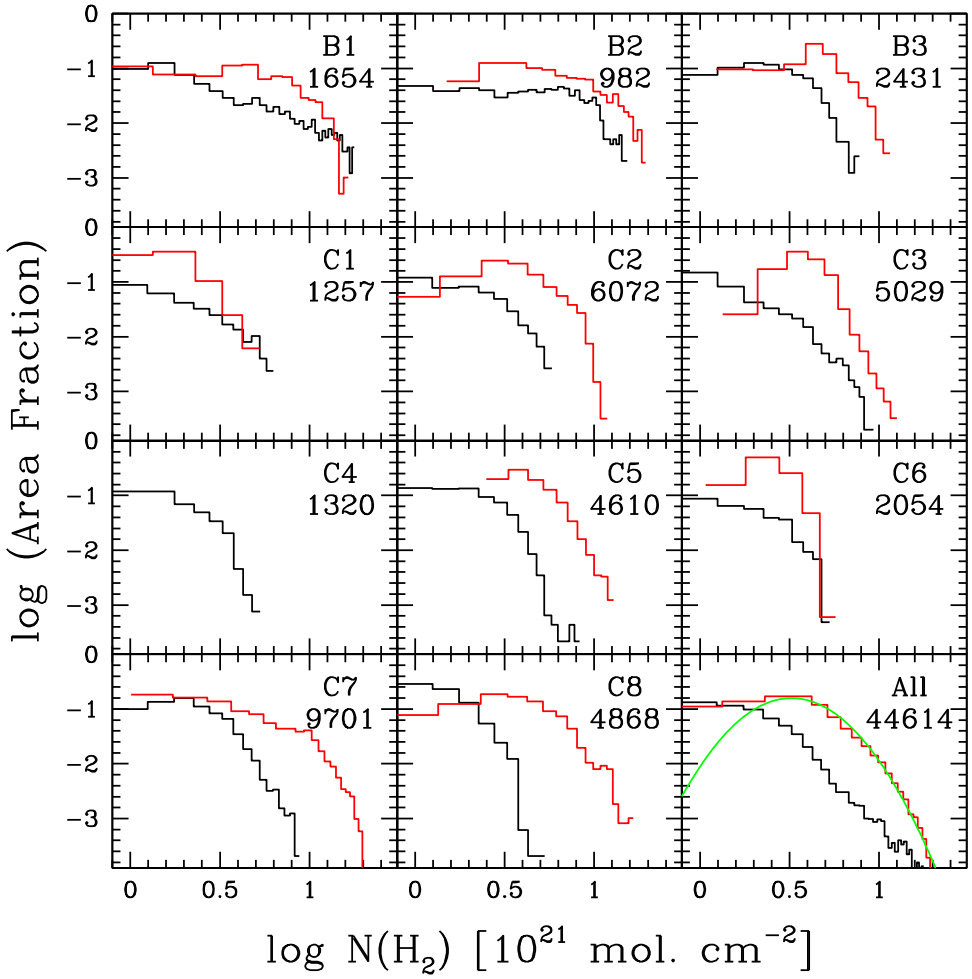

Figure 12. Histograms of (black) normalized area with H_2 column density, $N(H_2)$, derived by LTE analysis from CO and ^{13}CO $J = 2$–1 emission and (red) IR-derived A_V scaled by 9.43×10^{20} mol cm^{-2} mag^{-1} (assuming standard gas-to-dust and that all gas is molecular). The labels at the top right indicate subregions shown in Figures 3, 4, and 10. The numbers at the top right give the total number of $10'' \times 10''$ pixels in each black histogram. The green curve in the lower right panel illustrates a lognormal function that was fitted to the A_V data for $A_V > 3$ mag.

tightly clustered along the major axis of the ridge of higher column density gas, while the Class II objects are spread more widely around the central gas concentration. This trend in the distribution of Class I and II YSOs is similar to that found by Bieging et al. (2016) for the core of the Sh2-235 giant molecular cloud (GMC).

Following the analysis by Bieging et al. (2016) for Sh2-235, we examined the average YSO areal density as a function of the molecular column density. In Figure 17, we plot the number of YSOs (both Class I and Class II) contained within contours of constant gas mass surface density in bins of 50–100, 100–150, 150–200, ... , 350–400 $M_\odot$ pc^{-2}, normalized by the area contained within each bin. The squares show values with sufficient numbers of YSOs to make a statistically meaningful estimate. The four highest points, marked as crosses, have only one, two, or three YSOs in each bin and are therefore probably not statistically meaningful. The error bars shown are the fractional uncertainty as $\sqrt{N}/N$, where N is the number of YSOs in each bin. The dashed line shows the fit to the same kind of analysis for the Sh2-235 GMC by Bieging et al. (2016). They found that the data were well represented by a power law with index 1.63 for a range of $\Sigma_{\rm gas}$ from 100 to 1000 $M_\odot$ pc^{-2}. We make a linear regression to the three lowest points in Figure 17 and find that a power law with an exponent of 1.74 is a good fit over the range of 50–200 $M_\odot$ pc^{-2}, a power law with almost the same exponent as that found for the GMC core of Sh2-235. However, the points for the Cep B and C clouds lie about one order of magnitude higher than the fit for the Sh2-235 GMC. This difference may be a result of the different distances of the two molecular clouds. Sh2-235 is 2.0 kpc from the Sun, while Cep B and C are 0.7 kpc distant. Since the searches for YSOs employed very similar data sets for both clouds, the nearer region may have allowed us to identify YSOs to a lower limiting magnitude and therefore mass. The surface density of YSOs may appear higher for Cep B and C than for Sh2-235 because we detect many more fainter YSOs, thereby enhancing the areal density for the nearer cloud.

5. Discussion

5.1. Uncertainties in LTE Analysis

We justify our LTE analysis of the CO and ^{13}CO $J = 2$–1 maps based on the observed near equality of the brightness temperatures of the CO $J = 2$–1 and $J = 3$–2 maps over the areas common to both and convolved to have the same angular resolution. Since the CO lines are optically thick, the observed brightness temperatures should closely resemble the excitation temperatures of the two transitions. The near equality of the CO

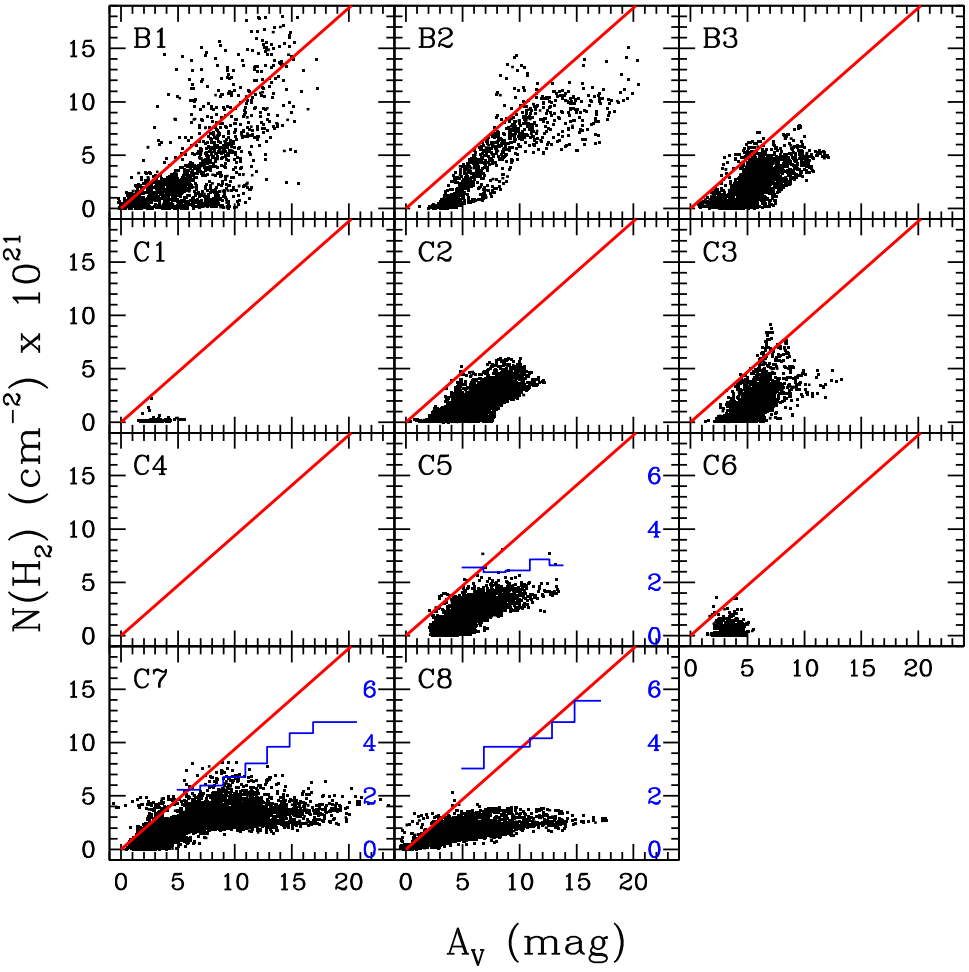

Figure 13. Scatter plots of $N(H_2)$ vs. A_V for each pixel within the subregions shown in Figures 3, 4, and 10. Region C4 lies outside the region mapped in A_V, so it is blank. Here $N(H_2)$ is derived from the LTE analysis of CO and ^{13}CO $J = 2$–1 maps with assumptions as described in the text. The diagonal red line shows the predicted relation if all H were molecular from a standard dust-to-gas ratio of 5.3×10^{-22} mag cm^2 H-nuclei^{-1} (Bohlin et al. 1978; Rachford et al. 2002; Draine 2011). For C5, C7, and C8, blue histograms show the depletion factors (defined in text and labeled in blue on right-side tick marks) for 2 mag wide bins in A_V.

brightness temperatures implies, then, that the lower rotational levels, $J \leqslant 3$, are in fact populated close to LTE conditions. With this justification, we can derive the excitation temperature (which we equate to the gas temperature) and the column density of the optically thin isotopologue, ^{13}CO, for the $J = 2$–1 transition. If LTE applies, we can calculate the partition function to derive the total column density $N(^{13}\mathrm{CO})$, summed over all rotational levels. (As noted in Section 4 above, in the lowest-density parts of the clouds, e.g., in an outer PDR layer, the lower rotational levels may not be fully thermalized, and ^{13}CO may be subthermally excited or selectively photodissociated compared to CO. Both effects will result in an overestimate of the total CO column density through such regions. Correcting for such effects would required detailed knowledge of the cloud structure, which is, however, not well constrained by the available data.)

There are, however, several additional, more or less certain assumptions needed to convert the column density $N(^{13}\mathrm{CO})$ to the total gas column density, including hydrogen and heavier elements. First, we make the commonly used assumption that $n(^{13}\mathrm{CO})/n(\mathrm{H_2}) = 2 \times 10^{-6}$, which was originally found by Dickman (1978) in a study of local dark clouds. This value seems to be appropriate for the molecular gas with visual extinction in the range 3 mag $\leqslant A_V \leqslant$ 10 mag, from a study of the Orion A and B clouds by Ripple et al. (2013). In this range of extinction, the gas is self-shielded from dissociation by ambient UV photons for both CO and ^{13}CO molecules, as well as H_2. They note, however, that a substantial amount of gas may be present in regions with $A_V < 3$ mag, where a PDR forms and reduces the abundance of CO and ^{13}CO relative to H_2. Moreover, because the two isotopologues differ in their photodissociation properties, the CO will self-shield to lower A_V than the ^{13}CO in the PDR layers. On the other extreme, for $A_V > 10$ mag, in the dense interior, if the gas and dust temperatures are $\leqslant$10 K, the isotopologues of CO will freeze out onto the grains, reducing the abundance relative to H_2. Ripple et al. (2013) estimated that in the Orion Molecular Cloud, these effects conspire so that assuming the "standard" value for $n(^{13}\mathrm{CO})/n(\mathrm{H_2})$ leads to a factor of 2 underestimate of the total molecular mass.

The ratio of isotopologues, $n(\mathrm{CO})/n(^{13}\mathrm{CO})$, does not directly affect our LTE analysis so long as the CO line is optically thick while ^{13}CO is not, with an optical depth $\leqslant$1. (As shown in the second panel of Figure 10, the ^{13}CO optical depth is in fact $<$1 over essentially the entire map.) The derived gas column density hinges on the $^{13}\mathrm{CO}/\mathrm{H_2}$ ratio, discussed above, but not on the isotope ratio. In a study of simulated turbulent clouds, Szucs et al. (2014) found that differential photodissociation is

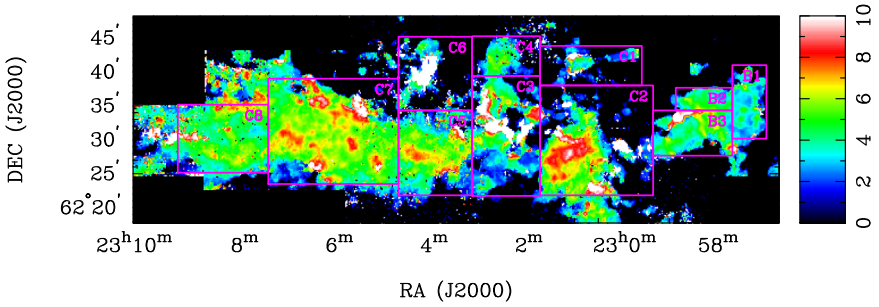

Figure 14. Map of sonic Mach numbers derived from LTE analysis. The color wedge is truncated at $M_s = 10$; pixels in white may have second velocity components that distort the ^{13}CO velocity dispersion.

less important than chemical fractionation in enhancing the ^{13}CO abundance and thereby affecting the inferred total gas mass. The effect is consistent with the conclusions of Ripple et al. (2013) that total gas mass may be underestimated by as much as a factor of 2.

One other assumption of importance is the gas-to-dust ratio. Although this does not directly affect our LTE analysis of the CO lines, the adopted standard extinction curve to convert IR colors to visual extinction (Section 2.3) could be in error for some lines of sight in the cloud. In effect, we have assumed the Galactic average ratio of total to selective extinction ($A_V/E_{B-V} = 3.1$). This value probably applies over the bulk of the Cep C cloud but may be affected in the vicinity of Cep B by the H II region Sh2-155. The optical-IR extinction curve can differ from the Galactic average for dust in the vicinity of H II regions (e.g., Whittet 2003; Draine 2011). Along such lines of sight, the conversion from *K*-band to *V*-band extinction is systematically in error; therefore, so is the gas column density derived from the A_V map (Figures 1 and 10). Such a systematic error might account, in part, for the anomalous points in subregions B1 and B2 in Figure 13, which is a scatter plot of $N(H_2)$ derived from the CO LTE analysis, versus the visual extinction from the stellar IR colors analysis (Section 2.3). Some points lie above the nominal relation between gas column density and visual extinction shown by the red line. If A_V is underestimated at these pixels due to a nonstandard reddening law, those points could be shifted to the left of the line, in contrast to almost all the other subregions, where deviations place points below the nominal line.

5.2. Cloud Structure and Variation of Properties with Position

From our LTE analysis, the total molecular mass of the Cep B and C clouds is $\sim$2000 $M_\odot$. Allowing for the effects of CO-dark gas in surrounding PDRs and possible CO depletion onto cold grains in dense interior regions, the actual mass may be a factor of 2 higher. As Sargent (1977) first noted, the Cepheus molecular cloud complex consists of several distinct components (or clumps, to use a commonly applied term). The total mass of the whole complex was estimated by Heyer et al. (1996) to be at least 18,000 $M_\odot$, so the Cep B and C clumps contain about 25% of the total. The largest gas surface densities are less by a factor of $\sim$5 than the peak surface densities we have found in other GMCs with substantially larger masses, e.g., Sh2-235 (Bieging et al. 2016), or for Orion A (Lada et al. 2013). The lack of high surface density regions is consistent with the observation that the fractional projected area of a cloud with surface density $\geqslant\Sigma_{\rm gas}$ is a sharply declining function of $\Sigma_{\rm gas}$ (Lada et al. 2013; Bieging et al. 2016). For a relatively low-mass cloud (or clump), then, only a very small fraction of the surface area is likely to have $\Sigma_{\rm gas} > 200\,M_\odot\,{\rm pc}^{-2}$.

Despite their modest total mass, the Cep B and C clouds exhibit a range of properties with position. The channel maps of CO and ^{13}CO have a complex structure, with a negative gradient in temperature from Cep B on the west end eastward to the extreme tip of Cep C. Cep B abuts the Cep OB3 association and its concentrated cluster of YSOs (Figure 18), and there is clear evidence that massive stars have recently formed in the interior of the Cep B cloud, specifically in subregion B1 (Felli et al. 1978; Kun et al. 2008; Nikoghosyan 2013). This distribution of massive young stars has been attributed to a triggering process driven by the effects of the recently formed members of Cyg OB3. To the west, the Cep C cloud is systematically colder and shows much less evidence of current star formation compared to Cep B. The main concentration of YSOs is on an elongated section of high column density in subregion C7.

The differences in molecular excitation between the two extremes of B1 and C7 are illustrated in Figure 18, which plots points at the observed peak brightness temperatures of ^{13}CO and CO in the $J = 2$–1 lines for all pixels within these two subregions for values of brightness temperature $>5\sigma$, or 0.5 K. The loci of constant excitation temperature (assumed to be the same for both isotopologues) are shown as the red curves. The green curves show the loci of constant CO optical depth under LTE conditions. The left panel, for subregion B1, shows that the range of excitation temperature (and therefore of gas kinetic temperature) is very broad, from $\sim$8 to 50 K, while the peak CO optical depths range from $\sim$5 to 50, with only a few pixels at higher optical depths. The wide range in temperatures must reflect the enhanced heating effects of the nearby OB stars and the embedded massive stars in the B1 subregion. In contrast, region C7 (right panel) shows a tight clustering of points between 10 and 20 K excitation temperature, with very few pixels at higher temperatures. The range of CO optical depths is larger than that in B1, with pixels up to $\tau = 100$, twice the upper envelope of optical depths for subregion B1. The distribution of pixels in this excitation parameter space implies that the molecular gas in C7 is cold and has areas of high gas column density, conditions that should be conducive to current star formation activity. This expectation is confirmed by the presence of many YSOs located along the high-extinction core where $A_V \geqslant 10$ mag (Figure 16), a grouping that suggests this is a small stellar cluster in formation.

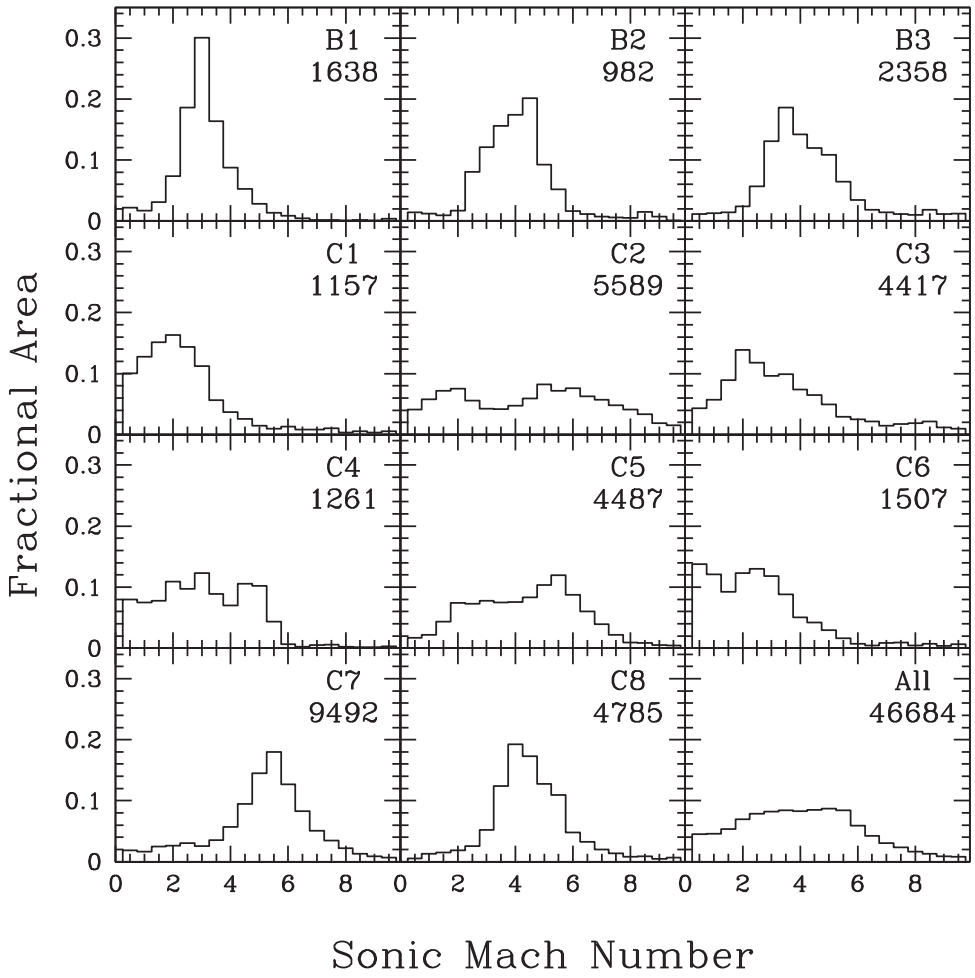

Figure 15. Distribution of sonic Mach numbers derived from LTE analysis for each of the 11 subregions shown in Figure 16 and the entire mapped field. Numbers at the upper right give the number of pixels in the histograms.

In their study of the Orion A and B GMCs (which employed observations and analysis similar to ours, except that they observed the $J = 1$–0 line of CO), Ripple et al. (2013) divided their maps into sections by galactic longitude and found significant variations between sections. We can also examine the correlations (or lack thereof) between some of the measured and derived properties, taken as spatial averages over the 11 subregions (B1–B3 and C1–C8), from values listed in Table 2. In Figure 19, we plot several correlations of averaged quantities. The trends are broadly consistent with the conclusions of Ripple et al. (2013) despite the considerable differences in cloud masses between Orion and Cep B/C. The three columns in Figure 19 show correlation plots versus ^{13}CO mean optical depth and CO mean excitation temperature, both derived from our LTE analysis, and versus $\langle A_V \rangle$ derived from the IR colors of background stars (Section 2.3). The top row of plots shows the quantity $\langle N(^{13}\mathrm{CO})/A_V \rangle$, which would be a constant if all gas on each line of sight were molecular with a constant $^{13}\mathrm{CO}/\mathrm{H_2}$ abundance ratio and the gas/dust ratio were constant, as well as the dust extinction curve. The vertical spread in each of the top three panels must result from deviations from these conditions. As Ripple et al. (2013) found, for low extinction regions ($A_V < 3$ mag), the gas is dominated by a PDR where CO and ^{13}CO are dissociated relative to H_2. The trend in the top center panel appears to be consistent with this effect. Likewise, the bottom center panel shows the nominal gas/dust relation (red line), and all points lie well below it. At low extinction, $N(\mathrm{H_2})$ is very low, likely because of dissociation of ^{13}CO in a PDR. At $\langle A_V \rangle \sim 5$ mag, the large spread in mean molecular column density may reflect a range of freeze-out of CO and ^{13}CO in cold, dense interiors. The right column of panels shows that most of the Cep C region has mean temperatures fairly tightly clustered between 12 and 15 K. The two regions with the highest mean excitation temperature are B1 and B2, where the molecular column densities are highest, and there are clear signs of recent and ongoing massive star formation.

Evidently, the variation in the mean properties of the molecular clouds reflects or results from the degree of recent star formation activity as a function of position in the cloud. Cep B has been actively forming stars, including massive ones, but Cep C so far has not formed OB stars, though some lower-luminosity YSOs are identified within it. It is not clear that there is sufficient gas at high column densities in Cep C to do so, unless future turbulent processes create more mass within high-density cores. Also, the appearance of Cep B and C suggests an elongated morphology where "triggering" might proceed from west to east. These two clouds are part of a larger complex, with six regions designated Cep A ... Cep F by Sargent (1977). Of these, Cep A has been well studied and

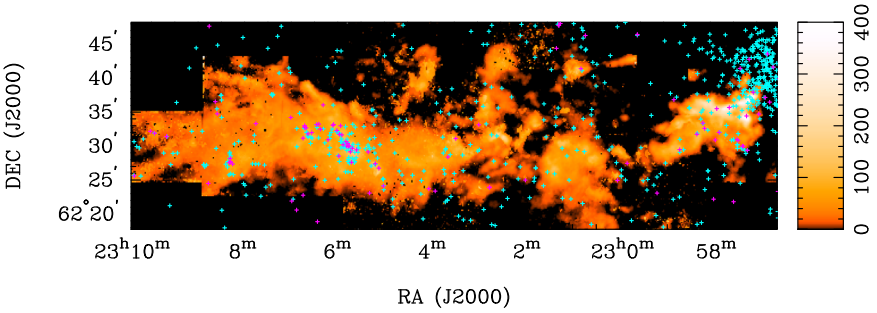

Figure 16. Positions of identified YSOs compared with total molecular gas surface density derived from LTE analysis (see Figure 10). Crosses mark YSOs of Class I (magenta) and Class II (cyan). The mass surface density color wedge is in $M_\odot$ pc^{-2} with logarithmic stretch. The cloud of points at the upper right is within the Cep OB3 association.

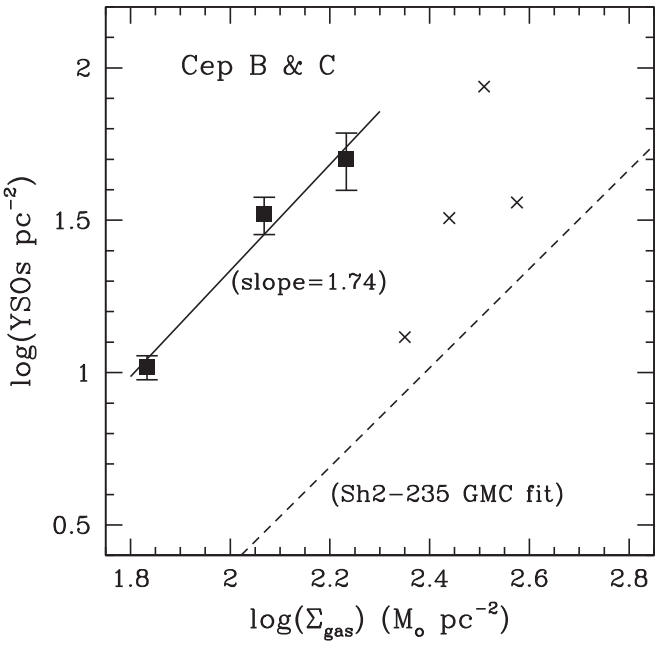

Figure 17. The YSO surface density averaged over bins in molecular gas surface density. Bins are at 50–100, 100–150, 150–200, etc., $M_\odot$ pc^{-2}. Only the lowest three bins have sufficient YSO content for statistically meaningful averages. Error bars show the fractional uncertainty as $\sqrt{N}/N$, where N is the number of YSOs in each bin. The crosses mark bins with only one or two YSOs and are not statistically meaningful. The solid line shows a fit to the three leftmost points. The dashed line (with a slope of 1.63) shows the fit derived by Bieging et al. (2016) for the giant molecular cloud associated with the H II region Sh2-235.

shows evidence of vigorous massive star formation. A triggering process of sequential star formation may be at work, though the observational evidence is perhaps not entirely compelling.

5.3. The CO X-factor

The integrated intensity of the CO $J = 1$–0 line, W(CO), has been used to derive total H_2 molecular column densities, $N(H_2)$, and from that, the masses of clouds by many authors. The so-called X-factor, defined as $X(\mathrm{CO}) \equiv N(H_2)/W(\mathrm{CO})$, gives the number of H_2 molecules cm^{-2} per K km s^{-1} of CO integrated line intensity. Essentially, all of these determinations use the $J = 1$–0 line of CO, which has the greatest coverage of clouds in the Galaxy. The column density of H_2 has been obtained by various means, including the total dust extinction, A_V (e.g., Paradis et al. 2012), and the flux of γ-rays produced by cosmic-ray interactions with hydrogen nuclei (Bloemen et al. 1986; Strong & Mattox 1996).

We have examined a form of the X-factor defined for the CO $J = 2$–1 transition using our observations of CO and our extinction map derived from IR colors of background stars. The observational definition is $X(\mathrm{CO\ 2–1}) \equiv N(H_2)/W(\mathrm{CO\ 2–1})$, where we take $N(H_2) = 9.43 \times 10^{20} A_V$ cm^{-2} assuming the standard gas-to-dust ratio (Draine 2011) and that all the gas is molecular. We calculated the value of X(CO 2–1) at each (unblanked) map pixel for the subregions B1–C8 shown above and the entire image. In Figure 20, we show histograms of each subregion, the mean value from the averages over each subregion ($\langle X(\mathrm{CO\ 2–1})\rangle = 9.43 \times 10^{20} \times \langle A_V\rangle/\langle W(\mathrm{CO\ 2–1})\rangle$), and the mean value of X(CO) from Paradis et al. (2012) derived for molecular gas in the solar vicinity using observations of the CO $J = 1$–0 line. If the CO $J = 2$–1 and 1–0 lines are optically thick and in LTE, the integrated line intensities should be nearly the same for a given line of sight. If this assumption is not strictly true, then comparing the value of X(CO 2–1) with that derived from the $J = 1$–0 line would require a correction factor that depends on the radiative transfer for each transition, which would depend on the detailed cloud geometry and spatial properties. Lacking this information, we assume here that the correction is of order unity.

In any case, the histograms in Figure 20 show that the distributions of X-factors vary significantly between different subregions, mostly showing a well-defined peak within a factor of 2 of the Paradis et al. (2012) value of 1.67×10^{20} H_2 cm^{-2}/(K km s^{-1}) but with a broad tail to larger values. These tails may contain ∼20%–40% of the total pixels. The peaks of the distributions are generally lower than the Paradis et al. (2012) average but vary from 1×10^{20} to 2×10^{20} H_2 cm^{-2}/(K km s^{-1}). Taking an average of A_V and W (CO 2–1) over each subfield, the ratio gives an (intensity-weighted) average X(CO 2–1) for each subfield that agrees with the Paradis et al. (2012) Galactic average to within about 20%. The distribution for the entire field, labeled "All," has a peak close to the Paradis et al. (2012) value but with a significant spread. This range of variation with location in the cloud is similar to the variation noted by Ripple et al. (2013) in the Orion A and B molecular clouds. They used maps of the $J = 1$–0 transitions of CO and ^{13}CO and extinction maps derived from 2MASS sky survey data using the same algorithm that we used, though with less-deep IR photometry.

The spread in the histograms of X(CO 2–1) probably reflects the existence of significant amounts of molecular gas that is "CO-dark" in the outer PDR layers of the cloud, with

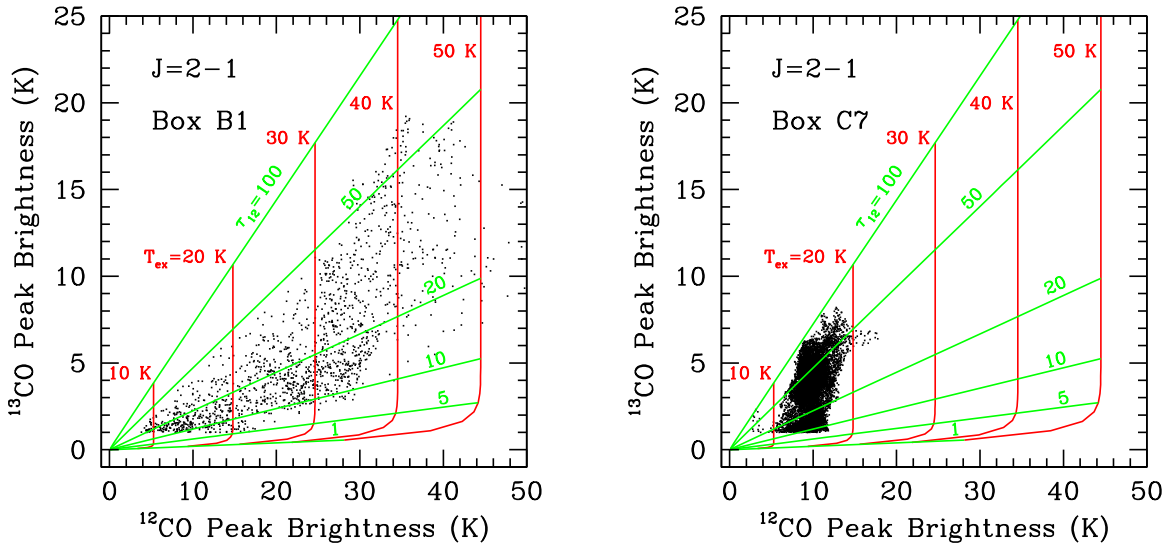

Figure 18. Scatter plots of CO vs. ^{13}CO peak brightness temperature for individual pixels in two contrasting subregions, box B1 (left) and box C7 (right). Colored lines show loci of constant $J = 2$–1 excitation temperature (T_{ex}) in red and constant CO $J = 2$–1 optical depth (τ_{12}) in green for LTE excitation conditions.

$A_V < 3$ mag, where CO is photodissociated while H_2 molecules are abundant. A lower abundance of CO should produce smaller values of W(CO 2–1) and hence higher values of X(CO 2–1) along sight lines through the PDR. At the other extreme, where $A_V > 10$ mag, in the dense, cold interior of clouds, CO will probably be frozen onto the grains, reducing the CO gas-phase abundance and therefore increasing the derived X(CO 2–1) value. For example, subregion C7 has a central area of high extinction but low gas temperature, as shown in Figure 10, so the long tail in the histogram of X(CO 2–1) may be largely a consequence of freeze-out of CO in the dense, cold interior. In contrast, the peak of the X(CO 2–1) histogram for subregion B1 is significantly lower than the galactic average of 1.67×10^{20} (Paradis et al. 2012). The high gas temperatures inferred from the CO LTE analysis would increase the average integrated line intensity, W(CO 2–1), compared to typical molecular cloud temperatures, thereby reducing the derived values of X(CO 2–1) for that subregion. Depletion of CO in B1 seems less likely to be important, given the relatively high gas temperatures we infer ($25\ \mathrm{K} < (T_{ex} \approx T_{kin}) < 40\ \mathrm{K}$) and assuming the gas and dust temperatures are well coupled. Photodissociation in the outer layers, given the likely enhanced UV photon flux from the nearby Cep OB3 association, could also play a role in raising the derived X(CO 2–1) values for sight lines near the hotter stars by reducing W(CO 2–1) as the CO/H_2 abundance is lowered. It appears, however, that the enhanced CO excitation temperatures largely outweigh CO destruction occurring in a PDR layer toward subregion B1.

5.4. YSO Surface Density versus Molecular Gas

The relationship between star formation and the surface density of star-forming gas has been a subject of study at least since Schmidt (1959) published his work concluding that the rate of star formation in galaxies varied as a power law of the total gas surface density raised to a power "between 1 and 2." Kennicutt & Evans (2012) reviewed the evidence for this relation for a wide selection of galaxies and found that, consistent with Schmidt's conjecture, the data are well fit by a power law with an exponent of 1.4 over at least 4 orders of magnitude in the disk-averaged gas surface density, Σ_{gas}, from 10 to $10^5\ M_\odot\ \mathrm{pc}^{-2}$ when averaging over entire galaxies. Other authors have emphasized the role of "dense" gas traced by HCN emission, for example (e.g., Gao & Solomon 2004), and found a nearly linear relation between the dense gas surface density and star formation rate.

Connecting the galaxy-averaged relation to the rate of star formation in individual molecular clouds is not straightforward. Ideally, one would like to take the total inventory of YSOs formed in a cloud or cloud complex over a known time interval, e.g., the cloud lifetime, and compare that with the average molecular gas column density as a function of position within the cloud. In practice, we can only find the YSOs that are present in a cloud now and compare their distribution with the molecular gas distribution as projected on the sky. In short, we have a "snapshot" of star formation at the current epoch but cannot follow the evolution of YSOs much beyond the classical T Tauri stage. Since YSOs presumably disperse from their natal crib over a few million years, the current distribution of the youngest stages, corresponding to Class I and II YSOs, probably gives the most faithful indication of current star formation in a given molecular cloud. In the GMC associated with Sh2-235, Bieging et al. (2016) found that the central $125\ \mathrm{pc}^2$ of the cloud showed a power-law relation between the surface density of Class I and II YSOs and the column density of molecular gas as derived from an analysis of the CO and ^{13}CO $J = 2$–1 emission identical to the analysis used in the present work. The best-fit power law from Bieging et al. (2016) is shown in Figure 17 as a dashed line and spans a range of gas surface densities from 100 to $1000\ M_\odot\ \mathrm{pc}^{-2}$. In the present work, we could extend the range of surface densities down to $50\ M_\odot\ \mathrm{pc}^{-2}$ with a statistically significant count of YSOs, as shown in Figure 17. For the lowest surface density range, from 50 to $200\ M_\odot\ \mathrm{pc}^{-2}$, the data also appear to follow a power law with an exponent of 1.74, very similar to that found by Bieging et al. (2016) for the Sh2-235 GMC. For surface densities above $200\ M_\odot\ \mathrm{pc}^{-2}$, the number of YSOs detected is too small to be statistically significant. This lack probably simply reflects that there are very few pixels in the field that have a molecular column density much above $\sim 10^{22}\ \mathrm{H_2\ cm}^{-2}$, which corresponds to a mass surface density of $200\ M_\odot\ \mathrm{pc}^{-2}$, as shown in

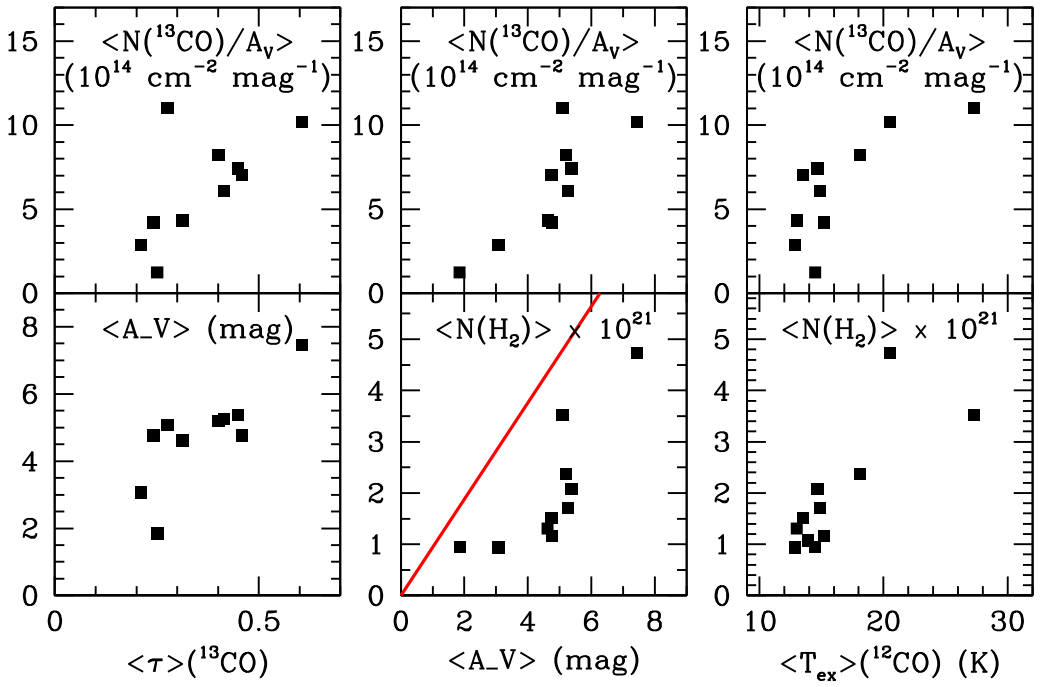

Figure 19. The LTE analysis properties averaged over the areas of boxes shown in Figures 3, 4, and 10 (see Table 1) and of A_V showing varying degrees of correlation. The red line shows the predicted relation if all H were molecular, from standard dust-to-gas ratio of 5.3×10^{-22} mag cm^2 H-nuclei^{-1} (Bohlin et al. 1978; Rachford et al. 2002; Draine 2011).

Figure 12. There are some pixels above this value in subfields B1 and B2, but those regions are in close proximity to the Cep OB3 cluster and the Sh2-155 H II region, so the star formation process in subregions B1 and B2 may have been disturbed by the effects of prior star formation, including OB stars.

In their study of the GMC associated with the H II region Sh2-235, Bieging et al. (2016) found a best-fit relation,

$$\Sigma(\mathrm{YSO}) = (2.3\ \mathrm{YSOs\ pc^{-2}}) \left(\frac{\Sigma_{\mathrm{gas}}}{100\ M_\odot\ \mathrm{pc^{-2}}} \right)^{+1.63},$$

where the fit covered the range 100–1000 $M_\odot$ pc^{-2}. (The mass includes a factor of 1.4 to account for helium and other elements.) In the present work, we find that the YSO surface density in the Cep B and C clouds obeys a power law with a similar exponent but an order-of-magnitude higher surface density, namely,

$$\Sigma(\mathrm{YSO}) = (22.\mathrm{YSOs\ pc^{-2}}) \left(\frac{\Sigma_{\mathrm{gas}}}{100\ M_\odot\ \mathrm{pc^{-2}}} \right)^{+1.74},$$

where the fit covers the range 50–200 $M_\odot$ pc^{-2}, and, as noted above, there is too little surface area with higher gas surface density to allow meaningful determination of YSO content for $\Sigma_{\mathrm{gas}} > 200\ M_\odot$ pc^{-2}. It is noteworthy that the two clouds have power laws with nearly the same slope. The difference of an order of magnitude in the normalization may be attributable to the nearer distance of Cep B and C (700 pc) compared to Sh2-235 (2.0 kpc). Since the IR photometric data from which YSOs are identified have similar limiting sensitivities, the nearer cloud may allow detection of YSOs an order of magnitude fainter and presumably also of lower mass.

In an earlier study, Gutermuth et al. (2011) used published catalogs of YSOs, together with maps of dust extinction derived from IR colors of background stars, to examine correlations between YSO and gas surface densities for a sample of eight star-forming molecular clouds within 1 kpc, including the Cep OB3 cloud. They included a larger area of the cloud complex than we have mapped here in CO. Remarkably, however, they concluded that their data were consistent with a power-law relation having an index of $+1.77 \pm 0.01$, virtually identical to our value for the combined Cep B and C regions shown in Figure 17. If we make the assumption used by Gutermuth et al. (2011) that the mean mass per YSO is 0.5 $M_\odot$, then our best fit from Figure 17 is in good agreement with their distribution of YSOs, especially for the Class I objects only, over the range of Σ_{gas} shown. It is reassuring that these two data sets, i.e., Gutermuth et al. (2011) and the present study, give such consistent results despite the very different observational material employed.

The power-law relations above could be transformed to a star formation rate versus gas surface density if we assume (1) a mean mass per detected YSO and (2) a timescale over which the observed YSOs have formed. It is difficult to determine the mass of individual YSOs directly from IR luminosities, since a star of a given mass undergoes significant evolution of luminosity and color during the pre-main-sequence phase. If we assume, as did Gutermuth et al. (2011), that the mean mass per detected YSO in the Sh2-235 sample is 0.5 $M_\odot$ and the timescale to produce these YSOs is 10^6 yr, the first of the above two power laws gives a star formation rate per kpc^2 that is nearly parallel to, but about one order of magnitude above, the relation shown by Kennicutt & Evans (2012) for disk averages of whole galaxies over the same range of gas surface densities. We argue that a timescale of 10^6 yr is reasonable because about half the YSOs in the Sh2-235 sample are Class I, and half are Class II. Heiderman & Evans (2015) found that the duration of the earliest stage of star formation, which we assume is the Class I objects, is 0.5 Myr, provided that the duration of the Class II phase is 2 Myr. Since

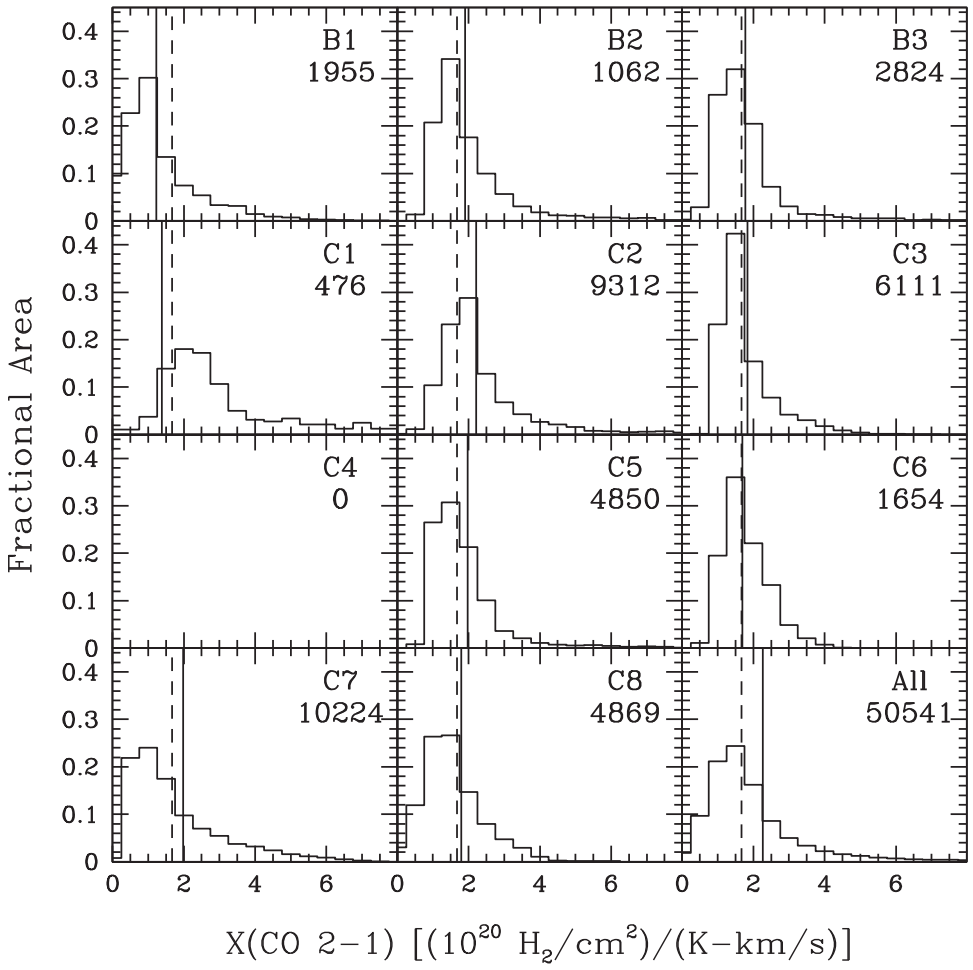

Figure 20. Histograms showing distributions of X(CO 2–1) within the subregions shown in Figures 3, 4, and 10. Subregion C4 lies outside the region mapped in A_V, so it is blank. The dashed vertical line shows the mean X(CO) for gas in the solar vicinity derived for the $J = 1$–0 line (Paradis et al. 2012). The solid vertical line shows the value calculated from the average over each subregion, i.e., $\langle X(\mathrm{CO\ 2\text{–}1})\rangle = \langle A_V\rangle/\langle W(\mathrm{CO})\rangle$. The number at the upper right shows the total pixel count in each histogram.

half the YSOs in the Sh2-235 sample are Class I, the timescale to form the observed young stars cannot be as long as 2 Myr, so an average age of 1 Myr is reasonable.

In contrast, comparing Sh2-235 with the second of the above relations for Cep B and C, we argue that the mean stellar mass for the Cepheus YSOs is likely lower, perhaps by a factor of 2 or 3, but may have a correspondingly longer mean age. (We do not have estimates of the YSO masses for our sample, only the IR color-determined class.) The uncertainties are large enough that it seems possible that the two samples may be consistent with the same star formation rate versus gas surface density law, at least over the range covered by the power-law fits. It may equally well be that these two examples of star-forming molecular clouds have intrinsically different relations between star formation surface density rates and molecular gas surface density. Lada et al. (2013) showed that there is a power-law relation within individual GMCs but that the normalization differs by at least an order of magnitude from cloud to cloud. They argued that differences in cloud structure are crucial to establishing the level of star formation activity. In massive GMCs, such as Orion A, a large surface area with high gas surface density (corresponding to $A_K > 0.9$ mag) engenders a high rate of star formation, while a cloud with relatively little area of high gas surface density produces few YSOs per unit surface area.

The overall Cep C cloud morphology is strikingly similar to that of Orion A (Stutz & Gould 2016): it is elongated with an approximate axial ratio of ∼1:4, and there is a well-known OB cluster (Cep OB3) at one end of the Cep B cloud, while at least one other cluster may be in the process of formation (in subregion C7). Our data do not probe the highest-density gas, whose presence is not only expected but suggested by the freeze-out of CO in the high-A_V regime of the colder regions (e.g., region C7). Our extinction map (Figure 1) suggests that there is a higher-density filament ridgeline where star formation is concentrated. On the western edge of the cloud, there is a high-density gas filament that appears directly associated with the Cep OB3 cluster and appears to be adding new stars into (the center of) the cluster (e.g., Hacar et al. 2017; Stutz 2018). Sensitive maps of N_2H^+, for example, might reveal the high-density gas that is presumably the site of current star formation (e.g., Stutz & Gould 2016). Such kinematic data would measure the velocities of the dense gas, testing cluster formation mechanisms in the Cep OB3 molecular cloud (e.g., Stutz & Gould 2016; Stutz 2018).

5.5. Isolated CO Globules

In Section 3.4, we discussed the detection of at least 17 isolated, compact CO sources detected in the $J = 3$–2 line,

which we list in Table 1. Here we speculate on the origin and nature of these objects. It seems unlikely that these small clouds formed in isolation and have persisted for any length of time. Probably these small clouds are the remnant cores from molecular gas that was compressed by supersonic turbulence but lacked sufficient mass to undergo gravitational collapse and form stars. We suspect that these are just borderline virially stable, but unless they somehow cool and/or are compressed to a sufficient density to become gravitationally unstable, they will disperse on at most several sound-crossing timescales. Assuming distances similar to the Cep B and C clouds (700 pc), these clouds have sizes of a few tenths of a parsec and may be similar to local Bok globules, or the "small molecular clouds" cataloged by Clemens & Barvainis (1988). Unfortunately, our lack of knowledge of accurate distances makes a calculation of virial stability uncertain. These compact clouds would, however, be of interest for further studies to better characterize their properties, likely origin, and future evolution.

6. Summary

Observational material. We have presented fully sampled maps of emission from the $J = 2$–1 transitions of CO and ^{13}CO and of the $J = 3$–2 transition of CO (but not ^{13}CO) over the Cep B and C molecular clouds, first identified by Sargent (1977). The angular resolution of the maps is 38″ (FWHM) after modest spatial smoothing to match all three data sets. The velocity resolution of the $J = 2$–1 maps is 0.3 km s^{-1}, and that of the $J = 3$–2 map is 0.23 km s^{-1}. We also present a map of the visual extinction, A_V, over nearly the same region and with similar angular resolution. The extinction was measured using a set of deep JHK_S images obtained with the Omega2000 camera at the Calar Alto Observatory and employing the NICEST technique (Lombardi 2009) to convert IR colors of background stars to K-band extinction. We assume a standard Galactic extinction law to convert A_K to A_V. Finally, we combine archival IR photometry from *Spitzer* and *WISE* together with new deep JHK_S IR photometric imaging using the CFHT to identify a catalog of YSOs and classify them by evolutionary category.

Data products. The calibrated CO and ^{13}CO image cubes of brightness temperature versus LSR velocity are made available for download as FITS files. The catalog of YSOs will be presented in a future publication.

Analysis and interpretation. Comparison of the brightness temperatures of the CO $J = 2$–1 and $J = 3$–2 maps shows that the CO rotational transitions must be populated close to LTE for $J \leqslant 3$; we argue that LTE is also a good assumption for the ^{13}CO lowest rotational levels. An LTE analysis yields maps of both the CO excitation temperature, which we equate with the gas kinetic temperature, and the ^{13}CO column density. Assuming a standard ^{13}CO/H$_2$ abundance ratio yields a map of the molecular gas column density over the whole mapped region.

The CO maps have multiple substructures with a range of physical properties that are related to the extent of recent star formation in or adjacent to these structures. We divide the maps into 11 subregions and examine various correlations within them. The distributions of H$_2$ column density for each subregion show relatively sharp cutoffs consistent with a nearly lognormal distribution for those areas with little or no sign of current star formation, while the regions within Cep B that show evidence of ongoing (massive) star formation have extended exponential-like tails to large molecular column densities. A pixel-by-pixel comparison of the molecular column density $N(H_2)$ derived from our CO LTE analysis with the IR color-derived A_V shows that for regions with low gas temperature at high extinction ($A_V > 10$ mag), the CO-derived molecular column densities are well below the Galactic average expected if all H were molecular and the ^{13}CO abundance were uniform throughout the cloud. We conclude that the observed deficit results from the depletion of CO from the gas via freeze-out onto cold grains in the dense cloud interiors.

We use the gas temperature from our LTE analysis together with the measured ^{13}CO line width to create a map of the sonic Mach number, a critical parameter in numerical models of gravo-turbulent star formation. The Mach numbers show significant variations from region to region and within the subregions, with typical values in the range 3–6 but everywhere $\geqslant 1$, consistent with the pervasive nature of supersonic turbulence within these clouds.

The distribution of YSOs of Classes I and II from our deep IR photometry reveals locations of current active star formation. We find that the surface density of YSOs is a power-law function of the molecular gas surface density inferred from our LTE analysis of CO, $50\,M_\odot\,\mathrm{pc}^{-2} \leqslant \Sigma_{\rm gas} \leqslant 200\,M_\odot\,\mathrm{pc}^{-2}$. Because the molecular mass of Cep B and C is not large while the areal distribution is a steeply declining function of $\Sigma_{\rm gas}$, there is very little surface area above $200\,M_\odot\,\mathrm{pc}^{-2}$ with too few YSO candidates to be statistically significant. The surface density of YSOs for $\Sigma_{\rm gas} \leqslant 200\,M_\odot\,\mathrm{pc}^{-2}$ is consistent with a power law of index $\sim$+1.7, very similar to that found by Bieging et al. (2016) for the GMC associated with the H II region Sh2-235.

We consider the uncertainties in the assumptions made in our LTE analysis. In particular, the assumption of a constant ^{13}CO/H$_2$ abundance along each line of sight clearly must break down in the outer layers of the clouds with $A_V < 3$ mag, where formation of a PDR reduces this abundance ratio to near zero. At the other extreme, in the cold, dense interiors of clouds, freeze-out of CO onto dust grains also reduces the CO (and ^{13}CO) abundance to very low values, where $A_V > 10$ mag. Our results are broadly consistent with those of Ripple et al. (2013) for the Orion A and B molecular clouds, which show that these two effects (PDR and freeze-out) may cause an LTE analysis to underestimate the true mass by a factor of $\sim$2.

We calculate a $J = 2$–1 CO X-factor as a function of position in the cloud. There is a broad distribution of values within each of the 11 subregions, but the (intensity-weighted) spatial averages of each are close to the Galactic mean value derived (from CO $J = 1$–0 emission) by Paradis et al. (2012) to within about 20%.

Finally, we find a significant number of compact, spatially isolated emission features in the CO $J = 3$–2 data cube and tabulate positions, velocities, and sizes for 17 of these well-isolated compact sources. There may be others that appear blended with more extended cloud emission. Since these compact sources are relatively bright in the $J = 3$–2 line, they must have modestly high gas temperatures. Without knowing the distances, we cannot calculate a virial stability parameter, but we speculate that these are marginally stable remnants of dense cores formed by gravo-turbulence and will likely disperse. We do not find associated YSOs from our new catalog.

The Heinrich Hertz Submillimeter Telescope is operated by the Arizona Radio Observatory, which is part of Steward Observatory at the University of Arizona. This work was supported in part by National Science Foundation grants AST-0708131 and AST-1140030 to the University of Arizona. We thank Dr. A. R. Kerr of the National Radio Astronomy Observatory for providing the ALMA prototype mixers used in this work. This project has received funding from the European Union's Horizon 2020 research and innovation program under grant agreement No. 639459 (PROMISE). AMS gratefully acknowledges funding support through the Fondecyt regular (project code 1180350), the "Concurso Proyectos Internacionales de Investigación, Convocatoria 2015" (project code PII20150171), and the Chilean Centro de Excelencia en Astrofísica y Tecnologías Afines (CATA) BASAL grant AFB-170002.

Appendix
Downloadable Data Files

The three calibrated FITS-format brightness temperature image cubes can be downloaded as "data behind the figure":

Figure 6, CO $J = 2$–1

Figure 7, ^{13}CO $J = 2$–1

Figure 9, CO $J = 3$–2.

The $J = 2$–1 data cubes have been resampled in velocity to have identical LSR velocities spaced by 0.3 km s^{-1}, slightly less than the resolution of the 0.25 MHz filter banks. The $J = 3$–2 data cube has velocity sampling at 0.233 km s^{-1}, the spectral resolution of the 64-beam array receiver. All of the images are in main-beam brightness temperature and have been convolved to the same angular resolution of 38″ (FWHM).

ORCID iDs

John H. Bieging https://orcid.org/0000-0002-6291-7805
Jouni Kainulainen https://orcid.org/0000-0001-7764-3109
Amelia M. Stutz https://orcid.org/0000-0003-2300-8200

References

Ballesteros-Paredes, J., Hartmann, L. W., Vázquez-Semadeni, E., Heitsch, F., & Zamora-Avilés, M. A. 2011, MNRAS, 411, 65
Bertin, E. 2006, in ASP Conf. Ser. 351, Astronomical Data Analysis Software and Systems XV, ed. C. Gabriel et al. (San Francisco, CA: ASP), 112
Bertin, E., & Arnouts, S. 1996, A&AS, 117, 393
Bertin, E., Mellier, Y., Radovich, M., et al. 2002, in ASP Conf. Ser. 281, Astronomical Data Analysis Software and Systems XI, ed. D. A. Bohlender, D. Durand, & T. H. Handley (San Francisco, CA: ASP), 228
Bieging, J. H., Patel, S., Peters, W. L., et al. 2016, ApJ, 226, 13
Bieging, J. H., & Peters, W. L. 2011, ApJS, 196, 18
Bieging, J. H., Revelle, M., & Peters, W. L. 2014, ApJS, 214, A7
Blaauw, A. 1964, ARA&A, 2, 213
Blaauw, A., Hiltner, W. A., & Johnson, H. L. 1959, ApJ, 130, 69
Bloemen, J. B., Strong, A. W., Mayer-Hasselwander, H. A., et al. 1986, A&A, 154, 25
Bohlin, R. C., Savage, B. D., & Drake, J. F. 1978, ApJ, 224, 132
Burkhart, B., Collins, D. C., & Lazarian, A. 2015, ApJ, 808, 48
Cardelli, J. A., Clayton, G. C., & Mathis, J. S. 1989, ApJ, 345, 245
Clemens, D. P., & Barvainis, R. 1988, ApJS, 68, 257
Dickman, R. L. 1978, ApJS, 37, 407
Draine, B. T. 2011, Physics of the Interstellar and Intergalactic Medium (Princeton, NJ: Princeton Univ. Press)
Federrath, C. 2018, PhT, 71, 38
Federrath, C., & Klessen, R. 2013, ApJ, 763, 51
Federrath, C., Klessen, R. S., & Schmidt, W. 2008, ApJL, 688, L79
Felli, M., Tofani, G., Harten, R. H., & Panagia, N. 1978, A&A, 69, 199
Fukui, Y., Iwata, T., Mizuno, A., Bally, J., & Lane, A. P. 1993, Protostars and Planets III (Tucson, AZ: Univ. of Arizona Press), 603
Gao, Y., & Solomon, P. M. 2004, ApJ, 606, 271
Getman, K. V., Feigelson, E. D., Luhman, K. L., et al. 2009, ApJ, 699, 1454
Getman, K. V., Feigelson, E. D., Townsley, L., et al. 2006, ApJS, 163, 306
Gutermuth, R. A., Megeath, S. T., Myers, P. C., et al. 2009, ApJS, 184, 18
Gutermuth, R. A., Pipher, J. L., Megeath, S. T., et al. 2011, ApJ, 739, 84
Hacar, A., Alves, J., Tafalla, M, & Goicoechea, J. R. 2017, A&A, 602, L2
Heiderman, A., & Evans, N. J., II 2015, ApJ, 806, 231
Hennebelle, P., & Falgarone, E. 2012, A&ARv, 20, 55
Heyer, M. H., Carpenter, J. M., & Ladd, E. F. 1996, ApJ, 463, 630
Kainulainen, J., Beuther, H., Henning, T., & Plume, R. 2009, A&A, 508, L35
Kainulainen, J., Federrath, C., & Henning, T. 2014, Sci, 344, 183
Kainulainen, J., Beuther, H., Federrath, C., & Henning, T. 2011, A&A, 530, A64
Kainulainen, J., Lehtinen, K., & Harju, J. 2006, A&A, 447, 597
Kennicutt, R. C., & Evans, N. J. 2012, ARAA, 50, 531
Kharchenko, N. V., Piskunov, A. E., Roeser, S., Schilbach, E., & Scholz, R.-D. 2005, A&A, 438, 1163
Klessen, R. 2000, ApJ, 535, 869
Kloosterman, J., Cottam, T., Swift, B., et al. 2012, Proc. SPIE, 8452, 845204
Koenig, X. P., & Leisawitz, D. T. 2014, ApJ, 791, 131
Kong, S., Lada, C. J., Lada, E. A., et al. 2015, ApJ, 805, 58
Kovacs, Z., Mall, U., Bizenberger, P., Baumeister, H., & Röser, H.-J. 2004, Proc. SPIE, 5499, 432
Kritsuk, A., Norman, M., & Wagner, R. 2011, ApJL, 727, L20
Kun, M., Kiss, Z. T., & Balog, Z. 2008, in The Handbook of Star-forming Regions, Vol. I: The Northern Sky, ed. B. Reipurth (San Francisco, CA, Dordrecht: ASP, Reidel), 1, ASP Monograph Publ., Vol. 4, 136
Lada, C. J. 2010, ApJ, 724, 687
Lada, C. J., Lombardi, M., Roman-Zuniga, C., Forbrich, J., & Alves, J. F. 2013, ApJ, 778, 133
Lauria, E. F., Kerr, A. R., Reiland, G., et al. 2006, ALMA Memo 553 (Charlottesville, VA: NRAO)
Lombardi, M. 2005, A&A, 438, 169
Lombardi, M. 2009, A&A, 493, 735
Lombardi, M., & Alves, J. 2001, A&A, 377, 1023
Lombardi, M., Alves, J., & Lada, C. J. 2015, A&A, 576, L1
Maret, S., Bergin, E. A., & Tafalla, M. 2013, A&A, 559, A53
Milam, S. N., Savage, C., Brewster, M. A., Ziurys, L. M., & Wyckoff, S. 2005, ApJ, 634, 1126
Nikoghosyan, E. H. 2013, Ap, 56, 165
Padoan, P., Federrath, C., Chabrier, G., et al. 2014, Protostars and Planets VI (Tucson, AZ: Univ. Arizona Press), 77
Padoan, P., Nordlund, A., & Jones, B.J.T. 1997, MNRAS, 288, 145
Paradis, D., Dobashi, K., Shimoikura, T., et al. 2012, A&A, 543, A103
Pineda, J. E., Caselli, P., & Goodman, A. A. 2008, ApJ, 679, 481
Rachford, B. L., Snow, T. P., Tumlinson, J., et al. 2002, ApJ, 577, 221
Reid, M. J., Menten, K. M., Brunthaler, A., et al. 2014, ApJ, 783, 130
Ripple, F., Heyer, M. H., Gutermuth, R., Snell, R. L., & Brunt, C. M. 2013, MNRAS, 431, 1296
Robitaille, T. P., Meade, M. R., Babler, B. L., et al. 2008, AJ, 136, 2413
Saral, G., Hora, J. L., Willis, S. E., et al. 2015, ApJ, 813, 25
Sargent, A. I. 1977, ApJ, 218, 738
Sargent, A. I. 1979, ApJ, 233, 163
Sault, R. J., Teuben, P. J., & Wright, M. C. H. 1995, in ASP Conf. Ser. 77, Astronomical Data Analysis Software and Systems IV, ed. R. Shaw, H. E. Payne, & J. J. E. Hayes (San Francisco, CA: ASP), 433
Schmidt, M. 1959, ApJ, 129, 243
Schneider, N., Andre, P., Konyves, V., et al. 2013, ApJL, 766, L17
Schneider, N., Bontemps, S., Motte, F., et al. 2016, A&A, 587, A74
Skrutskie, M. F., Cutri, R. M., Stiening, R., et al. 2006, AJ, 131, 1163
Strong, A. W., & Mattox, J. R. 1996, A&A, 308, 213
Stutz, A. M. 2018, MNRAS, 473, 4890
Stutz, A. M., & Gould, A. 2016, A&A, 590, A2
Stutz, A. M., & Kainulainen, J. 2015, A&A, 577, L6
Szucs, L., Glover, S. C. O., & Klessen, R. S. 2014, MNRAS, 445, 4055
Testi, L., Olmi, L., Hunt, L., Felli, M., & Goldsmith, P. 1995, A&A, 303, 881
Tremblin, P., Schneider, N., Minier, V., et al. 2014, A&A, 564, A106
Vazquez-Semadeni, E. 1994, ApJ, 423, 681
Veneziani, M., Piacentini, F., Noriega-Crespo, A., et al. 2013, ApJ, 772, 56
Whittet, D. C. B. 2003, Dust in the Galactic Environment (2th ed; Bristol: Institute of Physics Press)
Zhang, M., Kainulainen, J., Mattern, M., Fang, M., & Henning, T. 2018 A&A, submitted